MNRAS **000**, 000–000 (0000) Preprint 1st January 2019 Compiled using MNRAS LATEX style file v3.0

Energy Budget and Core-Envelope Motion in Common Envelope Evolution

Luke Chamandy,[1]★ Yisheng Tu,[1] † Eric G. Blackman, [1]‡ Jonathan Carroll-Nellenback,[1] §
Adam Frank,[1]¶ Baowei Liu[1] ‖ and Jason Nordhaus[2,3] ★★
[1]*Department of Physics and Astronomy, University of Rochester, Rochester NY 14618, USA*
[2]*National Technical Institute for the Deaf, Rochester Institute of Technology, NY 14623, USA*
[3]*Center for Computational Relativity and Gravitation, Rochester Institute of Technology, NY 14623, USA*

1st January 2019

ABSTRACT

We analyze a 3D hydrodynamic simulation of common envelope evolution to understand how energy is transferred between various forms, leading to the partial unbinding of the envelope. We find that 13–14% of the envelope is unbound during the simulation. Virtually all of the unbinding occurs before the end of the rapid plunge-in phase, here defined to coincide with the first periastron passage. In contrast, the total envelope energy is nearly constant during this time because positive energy transferred to the gas is counterbalanced by the negative binding energy from the closer proximity of the inner layers to the plunged-in secondary. During the subsequent slow spiral-in phase, energy continues to transfer to the envelope from the red giant core and secondary core particles. In our analysis, we critically assess the commonly used $\alpha_{\rm CE}$-energy formalism, and suggest an alternative that more cleanly separates core particles and gas. Applying this formalism, we discuss that overcoming current limitations of existing simulations with respect to both the accessible parameter regime and the giant model may enable complete envelope ejection from orbital evolution even without new energy sources. We also propose that relative motion between the centre of mass of the envelope and the centre of mass of the particles could account for the offsets of planetary nebula central stars from the nebula's geometric centre.

Key words: binaries: close – stars: evolution – stars: kinematics and dynamics – stars: mass loss – stars: winds, outflows – hydrodynamics

1 INTRODUCTION

In a binary stellar system, common envelope evolution (CEE) occurs when the envelope of a primary star, usually a giant, engulfs a smaller companion. Many astrophysical phenomena are believed to be preceded by one or more common envelope (CE) phases. Examples include asymmetric and bipolar planetary nebulae (PNe) and pre-PNe (PPNe), black hole (BH)-BH and neutron star (NS)-NS mergers, high- and low-mass X-ray binaries, and likely type Ia supernovae (SNe) (see Ivanova et al. 2013, for a recent review). Many observed binary systems have such small binary separations that they must be post-CE systems.

The so-called "energy formalism" (EF) was developed to predict the fate of a given binary system undergoing CEE and is useful for population synthesis studies (van den Heuvel 1976; Tutukov & Yungelson 1979; Livio & Soker 1988; de Kool 1990; Dewi & Tauris 2001). In this prescription, the two possible fates of CEE are merger or envelope ejection, depending on the value of an efficiency parameter $\alpha_{\rm CE}$, which is poorly constrained and cannot be reliably estimated from simulations if the envelope is not completely unbound (i.e. ejected). Thus far, 3D hydrodynamical simulations have yet to result in an ejected envelope unless an additional energy source (recombination energy) is introduced. However, the role of recombination is not yet universally agreed upon, in part because the released energy may be radiated away before it can be absorbed to contribute much to envelope ejection. In general, the absence of envelope ejection in simulations may also involve some combination of limitations of the theory (unjustified approximations, missing physics) or limitations of the simulations (unrealistic initial conditions, small duration, limited resolution, missing physics).

Due to the complexity and 3D morphology of CEE, global 3D models are useful. Early 3D hydrodynamical simulations of CEE were performed by Rasio & Livio (1996), who used smoothed particle hydrodynamics (SPH) and by Sandquist et al. (1998) and Sandquist et al. (2000), who used a finite difference code with nested

★ lchamandy@pas.rochester.edu
† ytu7@u.rochester.edu
‡ blackman@pas.rochester.edu
§ jcarrol5@ur.rochester.edu
¶ afrank@pas.rochester.edu
‖ baowei.liu@rochester.edu
★★ nordhaus@astro.rit.edu

grids. These papers analyzed the global energy budget and measured the amount of bound mass versus time.

More recent papers exploring the energy budget and mass unbinding include Passy et al. (2012), using a SPH code, Ricker & Taam (2012), using adaptive mesh refinement (AMR), and Ohlmann et al. (2016), using a moving mesh code. Our initial conditions herein closely match those of the latter to facilitate comparisons.

Iaconi et al. (2017) reviewed all previous simulations and compared SPH and AMR results, including a compilation of unbound mass for each simulation. Both Iaconi et al. (2017) and Iaconi et al. (2018) found that the unbound mass can increase as the resolution is enhanced in both AMR and SPH simulations. Iaconi et al. (2018) also found that the final fraction of unbound mass is generally larger for less massive envelopes or more massive secondaries.

The main goal of this work is to account for the various energy terms in our simulation as accurately as possible, and, in doing so, shed light on the envelope ejection process. How does the energy transition from one form to another with time? What are the expectations for envelope removal and energy transfer from analytic theory based on the EF, and to what extent do these expectations agree with simulation results? What strategies should be prioritized to achieve envelope ejection in future simulations?

In Sec. 2 we describe the simulation methods and setup. We analyze the global energy budget in Sec. 3. In Sec. 4, we explore how and to what extent the envelope becomes unbound. Sec. 5 focusses on the relative motion between the gas and particles, its effect on envelope unbinding, and implications for explaining observed offsets of some PN central stars from the geometric centres of their nebulae. In Sec. 6, we critically assess the standard EF used to understand CEE, and develop an alternative approach which we then use to interpret our simulation results. In Sec. 7 we discuss limitations of our simulation and CE simulations in general, along with future directions. We conclude in Sec. 8.

2 SIMULATION OVERVIEW

The simulation that we analyze here is Model A of Paper I, which involves the interaction of a $2.0\,\mathrm{M}_\odot$ red giant (RG) primary with a $0.4\,\mathrm{M}_\odot$ point particle core and a $1.0\,\mathrm{M}_\odot$ point particle representing a white dwarf (WD) or main sequence (MS) secondary. Unlike Model B of that paper, Model A did not have a subgrid model for accretion onto the secondary and Model A is simpler in that respect. See Paper I for a detailed description of the simulation setup which we summarize here.

The 3-D hydrodynamic simulation utilized the 3D AMR multi-physics code AstroBEAR (Cunningham et al. 2009; Carroll-Nellenback et al. 2013), and accounts for all gravitational interactions (particle–particle, particle–gas, and gas–gas). The RG density and pressure profiles were initialized similarly to that outlined by Ohlmann et al. (2017) (see Paper I), namely with the stars undergoing a circular orbit at $t = 0$ with orbital separation $a|_{t=0} = 49.0\,\mathrm{R}_\odot$, slightly larger than the RG radius of $R_1 = 48.1\,\mathrm{R}_\odot$. The simulation was terminated at $t = 40\,\mathrm{d}$. The mesh was refined at the highest level with voxel dimension $\delta = 0.14\,\mathrm{R}_\odot$ before $t = 16.7\,\mathrm{d}$ and $\delta = 0.07\,\mathrm{R}_\odot$ thereafter *everywhere* inside a large spherical region centered on the point particles. The initial radius of this maximally resolved region was $r_{\rm refine} = 72\,\mathrm{R}_\odot$ and at all times $r_{\rm refine} > 2.5a$. The spline softening radius for both particles was set to $r_{\rm soft} \approx 17\delta$ for the entire simulation. The base resolution used was $2.25\,\mathrm{R}_\odot$, and a buffer zone of 16 cells allowed the resolution to transition gradually between base and highest resolution regions. The box dimension is $1150\,\mathrm{R}_\odot$ and no envelope material reaches the boundary by the end of the simulation.

3 ENERGY BUDGET

We write the total energy $E_{\rm tot} = E_{1-2} + E_{\rm gas}$. Here E_{1-2} is particle orbital energy and is equal to the sum of particle kinetic energy $E_{\rm bulk,1} + E_{\rm bulk,2}$ and mutual potential energy of particles $E_{\rm pot,1-2}$. Complementally, the *binding* energy $E_{\rm gas}$ is defined as the sum of the gas-particle potential energy $E_{\rm pot,gas-1} + E_{\rm pot,gas-2}$ plus the gas-only contribution $E_{\rm bulk,gas} + E_{\rm int,gas} + E_{\rm pot,gas-gas}$. Since the binding energy is negative, transferring energy from E_{1-2} to $E_{\rm gas}$ would make $E_{\rm gas}$ less negative, and the gas less bound. In what follows, 'increase' of energy means toward more positive (or less negative) values, while 'decrease' means toward less positive (or more negative) values.

To alleviate confusion from previous literature, we include gas-particle potential energy and gas bulk kinetic energy in $E_{\rm gas}$, *not* in E_{1-2}. By doing so, we can characterize the problem in terms of transfer between "particle energy" and "gas energy". The theory is addressed further in Sec. 6 but here we focus on simulation results.

In the top panel of Fig. 1 we show the time-evolution of each energy component integrated over the simulation domain. Apastron and periastron passages are labeled on the time axis by long cyan or short magenta tick marks respectively. Expressions for the various contributions and their values at $t = 0$, $t = 13\,\mathrm{d}$ and $t = 40\,\mathrm{d}$, are given in Tab. 1. Time $t = 13\,\mathrm{d}$ is approximately that of first periastron passage and conveniently delineates the transition between the end of the plunge-in phase and the beginning of the slow in-spiral.[1] The inter-particle separation evolves from $a = 49.0\,\mathrm{R}_\odot$ at $t = 0$ to $a = 14.1\,\mathrm{R}_\odot$ at $t = 13\,\mathrm{d}$ and $a = 7.8\,\mathrm{R}_\odot$ at $t = 40\,\mathrm{d}$ (Paper I).

A key result from Fig. 1 (top) and Tab. 1 is that the potential energy term $E_{\rm pot,gas-2}$ is important even when the secondary is situated outside the RG surface at $t = 0$ and by the end of plunge-in at $t = 13\,\mathrm{d}$ comprises almost half of the gas potential energy.

The net energy transferred to $E_{\rm gas}$ from $t = 0$ until $t = 13\,\mathrm{d}$ is negligible even though almost all of the envelope unbinding occurs during this time (Sec. 4). The reason is that although the plunge-in of the secondary violently disrupts and energizes the outer layers of the envelope, it moves the secondary deeper in the envelope and more tightly binds it. The gain in gas kinetic energy is offset by the potential energy becoming more negative, and therefore negligible net exchange between particle energy and gas energy from the start of the simulation up to the end of plunge-in.

Complementally, owing to the continuous and highly variable gravitational force exerted on the particles by the gas, the total particle kinetic energy increases by almost as much as their mutual potential energy decreases between $t = 0\,\mathrm{d}$ and $t = 13\,\mathrm{d}$, resulting in almost zero net change in particle orbital energy.

Subsequently, after $t \approx 15\,\mathrm{d}$, energy is transferred from particle energy to gas energy at a roughly constant rate as the particles spiral in closer together. In the subsections below we expand on these points and discuss each of the curves in the top panel of Fig. 1 in detail.

[1] These phases are *loosely* equivalent to the dynamical plunge-in and self-regulating spiral-in phases discussed in Ivanova et al. (2013).

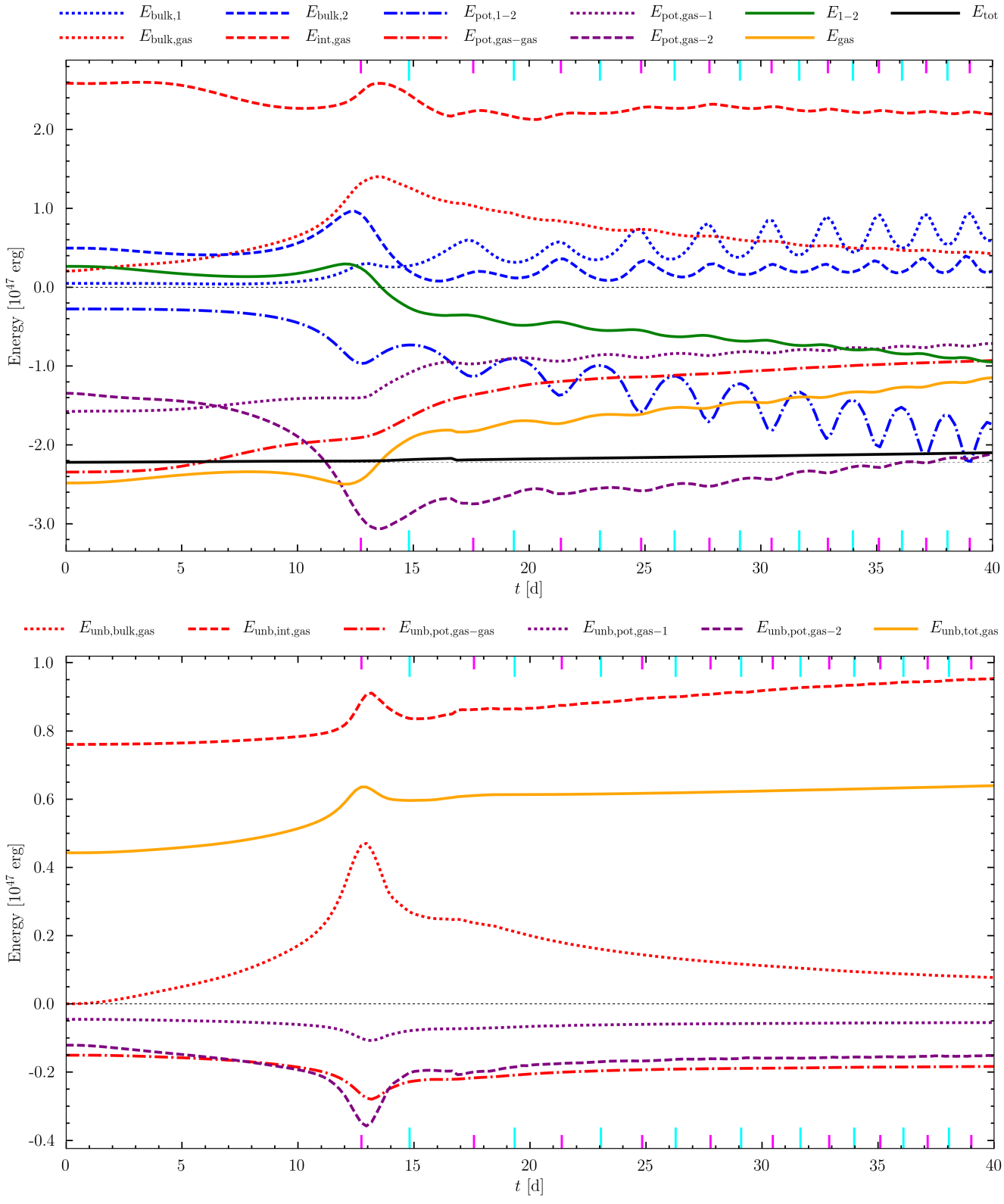

Figure 1. Top: Evolution of the various energy components integrated over the simulation domain (see Tab. 1 for symbol definitions). Those terms involving only particles are plotted in blue, only gas in red, and those involving gas and particles are plotted in mauve. Total energy is shown by a black line, with its initial value plotted as a grey dashed line for reference. Green and orange solid lines show the total particle and gas energies, respectively, with terms involving both particles and gas counting toward the total gas energy. A discontinuity at $t = 16.7$ d is caused by the change in the spline softening length of both particles from $2.4\,\mathrm{R}_\odot$ to $1.2\,\mathrm{R}_\odot$. The sampling rate of the data plotted is about one frame every 0.23 d. Times of apastron and periastron passage are shown as long cyan and short magenta tick marks, respectively. *Bottom:* As in the top panel but now showing the energy of the unbound gas only, where 'unbound' is defined as $\mathcal{E}_{\rm gas} \geqslant 0$. Note the difference in vertical axis range compared to the top panel.

Table 1. Terms in the energy budget, in units of 10^{47} erg, integrated over the simulation domain. Values are shown for the start of the simulation at $t = 0$, end of plunge-in at $t = 13$ d, and end of the simulation at $t = 40$ d. Also shown are the changes in the values between these times. For ease of presentation, expressions involving the gas–particle interactions neglect the modification of the particle potential at distances from the particle less than the spline softening length, but the values quoted were obtained using the full expressions for the potential.

Energy component	Symbol	Expression	$t = 0$	$t = 13$ d	$t = 40$ d	$\Delta E_{0-13\,\mathrm{d}}$	$\Delta E_{13-40\,\mathrm{d}}$	$\Delta E_{0-40\,\mathrm{d}}$
Particle 1 kinetic	$E_{\mathrm{bulk},1}$	$\frac{1}{2}M_{1,\mathrm{c}}v_{1,\mathrm{c}}^2$	0.05	0.30	0.59	0.25	0.29	0.54
Particle 2 kinetic	$E_{\mathrm{bulk},2}$	$\frac{1}{2}M_2 v_2^2$	0.49	0.86	0.20	0.37	−0.66	−0.29
Particle-particle potential	$E_{\mathrm{pot},1-2}$	$-\mathrm{G}M_{1,\mathrm{c}}M_2/a$	−0.28	−0.96	−1.74	−0.69	−0.78	−1.46
Gas bulk kinetic	$E_{\mathrm{bulk,gas}}$	$\frac{1}{2}\int\rho(\boldsymbol{x})v_{\mathrm{gas}}^2(\boldsymbol{x})\mathrm{d}V$	0.20	1.35	0.42	1.15	−0.93	0.22
Gas internal	$E_{\mathrm{int,gas}}$	$\frac{3}{2}\int P(\boldsymbol{x})\mathrm{d}V$	2.59	2.53	2.19	−0.06	−0.33	−0.39
Gas-gas potential	$E_{\mathrm{pot,gas-gas}}$	$\frac{1}{2}\int\Phi_{\mathrm{gas}}(\boldsymbol{x})\rho(\boldsymbol{x})\mathrm{d}V$	−2.35	−1.90	−0.93	0.45	0.97	1.41
Gas-particle 1 potential	$E_{\mathrm{pot,gas}-1}$	$-\mathrm{G}M_{1,\mathrm{c}}\int(\rho(\boldsymbol{x})/\lvert\boldsymbol{x}-\boldsymbol{x}_{1,\mathrm{c}}\rvert)\mathrm{d}V$	−1.58	−1.40	−0.72	0.18	0.68	0.86
Gas-particle 2 potential	$E_{\mathrm{pot,gas}-2}$	$-\mathrm{G}M_2\int(\rho(\boldsymbol{x})/\lvert\boldsymbol{x}-\boldsymbol{x}_2\rvert)\mathrm{d}V$	−1.35	−2.99	−2.12	−1.64	0.87	−0.77
Particle total	E_{1-2}	$E_{\mathrm{bulk},1}+E_{\mathrm{bulk},2}+E_{\mathrm{pot},1-2}$	0.26	0.20	−0.95	−0.06	−1.15	−1.21
Gas total	E_{gas}	$E_{\mathrm{bulk,gas}}+E_{\mathrm{int,gas}}+\sum_j E_{\mathrm{gas-j}}$	−2.49	−2.40	−1.15	0.08	1.25	1.33
Total	E_{tot}	$E_{1-2}+E_{\mathrm{gas}}$	−2.22	−2.20	−2.10	0.02	0.10	0.12

3.1 Total energy

The total energy is plotted in solid black in Fig. 1 and changes by 5% between $t = 0$ and $t = 40$ d (a dotted horizontal grey line shows the initial value for reference). The total energy rises gradually, except for a dip after $t = 16.7$ d when the softening radius around both particles and the smallest resolution element δ, were halved. This discontinuity is expected because reducing the spline softening radius from $r_{\mathrm{soft}} = r_{\mathrm{soft},0}$ to $r_{\mathrm{soft}} = r_{\mathrm{soft},0}/2$ immediately strengthens the gravitational force for $r < r_{\mathrm{soft},0}$. About 16% of the net increase in energy during the simulation is caused by inflow of the ambient medium from the domain boundaries. The remaining error in energy conservation might be caused numerically by the finite time step, which leads to particle orbits that are not completely smooth, or by errors introduced by the multipole Poisson solver. This small variation in the total energy does not affect the conclusions of the present study.

3.2 Particle and gas contributions

The solid green and solid orange lines in the top panel of Fig. 1 show the particle energy E_{1-2} and gas energy E_{gas}, respectively. The quantity E_{1-2} is the sum of the quantities shown by the blue curves, namely the kinetic energies of both particles and their mutual potential energy. $E_{1-2} > 0$ at $t = 0$ even though the binary system is bound because E_{1-2} does not include the contribution from $E_{\mathrm{pot,gas}-2}$. E_{gas} is equal to the sum of the quantities shown by the red and mauve curves pertaining to gas–only and gas–particle energy terms, respectively. The sum $E_{1-2} + E_{\mathrm{gas}} = E_{\mathrm{tot}}$ is shown in solid black. The green and orange curves show how the orbital energy of the particles is gradually transferred to the gas once the plunge-in phase ends.

To explain the energy evolution in greater detail, we now discuss the relationships between individual energy terms.

3.2.1 *Particles*

Energy terms pertaining to the particles only (RG core primary, labeled with subscript '1' and hereafter referred to as 'particle 1,' and secondary, labeled with subscript '2' and hereafter referred to as 'particle 2') are shown in blue. The kinetic energy of particle 1, $E_{\mathrm{bulk},1}$ (dotted blue), first remains steady and then gradually rises as the inter-particle separation reduces. It oscillates approximately synchronously with the orbit, with maxima in kinetic energy coinciding with periastron passages. The kinetic energy of particle 2, $E_{\mathrm{bulk},2}$ (dashed blue), first increases during the plunge-in phase from $t = 8$ and $t = 13$ d. This $E_{\mathrm{bulk},2}$ then decreases as the secondary migrates from having orbited the larger RG (core+envelope) mass to orbiting primarily only the smaller mass of particle 1. Following this decrease, $E_{\mathrm{bulk},2}$ then rises less rapidly than $E_{\mathrm{bulk},1}$, as there is continued competition between reduced particle separation and reduced gas mass interior to the orbit. Naturally, $E_{\mathrm{bulk},2}$ oscillates in phase with $E_{\mathrm{bulk},1}$.

The potential energy of particles $E_{\mathrm{pot},1-2}$ (which excludes that from gas–particle gravitational forces) is shown in dash-dotted blue, and its mean value over an orbit period reduces by 1.7×10^{47} erg between $t = 0$ and $t = 40$ d. $E_{\mathrm{pot},1-2}$ steadily decreases at $t = 40$ d, even as the rate of change of the mean inter-particle separation $\dot{\bar{a}}(< 0)$ (where bar denotes mean) reduces in magnitude (Paper I) so that $\ddot{\bar{a}} > 0$. This behaviour is expected from the $1/a$ Newtonian potential; for a circular orbit this gives $\dot{E}_{\mathrm{pot},1-2} \propto \dot{a}/a^2$ so the decrease in $|\dot{a}|$ competes with the reduction in a. Whether $\ddot{E}_{\mathrm{pot},1-2}$ is positive or negative depends on the details of orbital evolution.

3.2.2 *Gas*

Energy terms pertaining to gas only are shown in red in Fig. 1. The total bulk kinetic energy of gas $E_{\mathrm{bulk,gas}}$ (dotted red) rises during plunge-in as envelope material is propelled outward and then gradually reduces as gravity and shocks decelerate the envelope. The dashed red curve shows the internal energy of the gas $E_{\mathrm{int,gas}}$, of which about 0.8×10^{47} erg comes from the ambient medium. The latter has a pressure of 1×10^5 dyn cm^{-2} and fills the simulation domain. The ambient medium hardly contributes to $E_{\mathrm{bulk,gas}}$ however. $E_{\mathrm{int,gas}}$ is initially fairly steady, but then incurs modest variations from gas expansion and compression. Both $E_{\mathrm{int,gas}}$ and $E_{\mathrm{bulk,gas}}$ show small-amplitude oscillations with maxima approximately coinciding with periastron passages.

Each close encounter of the particles dredges up material in dual spiral wakes. During plunge-in, the gas acquires mostly bulk kinetic energy, but also significant internal energy, as expected from the observed spiral shocks. The subsequent slow decrease of

$E_{\rm bulk,gas}$ is accompanied by an increase in potential energy from gas self-gravity $E_{\rm pot,gas-gas}$ (dash-dotted red). Of the total $E_{\rm pot,gas-gas}$, the gravitational interaction between the ambient medium and envelope and that of the ambient medium with itself respectively contribute the relatively small amounts of 0.2×10^{47} erg and 0.1×10^{47} erg. Between $t = 0$ and $t = 40$ d, substantial work (1.4×10^{47} erg) is done expanding the envelope against its own gravity. In principle, unbinding the gas from the particles does not require the gas to become unbound from *itself*, but much of the energy acquired by the envelope in the simulations is drained into expansion against its own self-gravity.

3.2.3 *Gas-particles interaction*

The mauve curves in Fig. 1 show the potential energy terms accounting for the gas–particle 1 gravitational force $E_{\rm pot,gas-1}$ (dotted mauve) and gas–particle 2 gravitational force $E_{\rm pot,gas-2}$ (dashed mauve). These terms must be included in assessing the extent to which the envelope is bound. The ambient medium contributes negligibly to them ($< 0.2\times10^{47}$ erg total).

Initially the inner layers of the RG are hardly affected by interaction with the secondary, and so $E_{\rm pot,gas-1}$ varies slowly until the plunge-in, when the inner envelope is strongly disrupted. After the end of the plunge-in at $t = 13$ d, $E_{\rm pot,gas-1}$ increases with time as work is done to expand the envelope against the gravitational force from particle 1, situated roughly at its centre.

The gravitational interaction between gas and particle 2 (dashed mauve) is a bit more subtle and not fully accounted for in previous analyses using the CE energy formalism. Even at $t = 0$, $E_{\rm pot,gas-2}$ is important, being almost equal to $E_{\rm pot,gas-1}$ because particle 1 is closer to the bulk of the gas even though particle 2 is more massive. However, as particle 2 plunges toward the envelope centre, $E_{\rm pot,gas-2}$ increases in magnitude by 1.6×10^{47} erg and by $t = 13$ d becomes the most important contribution to the gas potential energy. From $t = 0$ until the end of plunge-in, $E_{\rm gas}$ gains only 0.1×10^{47} erg, or about 3%. This highlights that the liberation of orbital energy as particle 2 plunges in does not come "for free" because when M_2 arrives close to the envelope centre, the envelope is bound inside a much deeper potential well. During plunge-in, the energy liberated by $E_{\rm pot,gas-2}$ becoming more negative is transferred to the bulk kinetic energy of gas. Part of this kinetic energy does work to expand the envelope against gravity, as evidenced by increases in the gas-particle 1 and gas-gas potential energies.

From $t = 13$ d to $t = 40$ d, the envelope then expands to become less bound at the expense of the gas kinetic energy (dotted red) and particle–particle potential energy (dash-dotted blue) and significant work is expended on moving gas outward against self-gravity and the gravitational forces of particle 2 and particle 1.

4 PARTIAL ENVELOPE UNBINDING

We delineate gas as 'unbound' if its total energy density, $\mathcal{E}_{\rm gas} = \delta E_{\rm gas}/\delta V \geqslant 0$, where $\mathcal{E}_{\rm gas}$ equals the sum of bulk kinetic, internal and potential (due to self-gravity and interactions with both particles) energy densities.

As we explain below, virtually all of the unbinding of gas occurs between the start of the simulation and end of the plunge-in phase. As will become apparent in Sec. 4.2, this happens in spite of the negligible total energy transfer between particle orbital energy and gas binding energy (Sec. 3), but can be explained by recognizing that the nature and relative importance of energy exchange between various forms depends strongly on position.

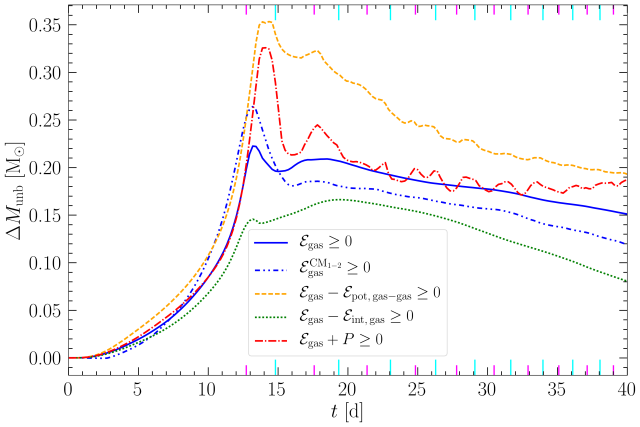

Figure 2. Change in unbound mass of the envelope with time according to the fiducial definition of 'unbound,' $\mathcal{E} \geqslant 0$ (solid blue), as well as various alternative definitions labeled in the legend (see Sec. 4).

4.1 Unbound mass

In Fig. 2 we plot the change in the unbound mass (defined by $\mathcal{E}_{\rm gas} \geqslant 0$) as a function of time (solid blue), not including the unbound ambient gas that inflows through the domain boundaries. Note that most of the ambient medium is already unbound at $t = 0$ (about 1.7 M$_\odot$). Only a small amount of ambient mass is bound at $t = 0$ (< 0.04 M$_\odot$), and while some of this bound mass may become unbound during the course of the simulation, its contribution to Fig. 2 would be negligible. In principle there could also be a small negative contribution from unbound ambient mass becoming bound, but data from 2D slices suggests that unbound ambient material, located at a distance $\gtrsim 200$ R$_\odot$ from particle 1, generally remains unbound. Therefore, the change in unbound mass $\Delta M_{\rm unb}$ plotted in Fig. 2 corresponds quite closely to the unbinding of bound envelope material.

The unbound mass increases from the start of the simulation until the end of plunge-in, then reduces slightly, recovers, levels off at $t \approx 17$ d, and then decreases steadily after $t \approx 19$ d. The steady decrease is caused by energy transferred from the envelope to the ambient medium. We estimate the total energy transfer in Sec. 4.3. As the ambient material has fairly large density and pressure in our simulation, this decrease is not seen in most other simulations. In nature, a circumbinary torus formed during the Roche-lobe overflow (RLOF) phase would be present and likely produce a similar effect. A peak in the unbound mass near the first periastron and a subsequent levelling off is also seen in the PHANTOM simulation of Iaconi et al. (2017) (see their Fig. 9, top panel for results from the run with the most comparable setup to ours; see also Iaconi et al. 2018), and other CEE simulations (Sandquist et al. 2000; Passy et al. 2012; Nandez et al. 2014). However, in Ricker & Taam (2012), unbinding peaks near the first periastron but continues for several orbits until the end of the simulation. In Sandquist et al. (1998), unbinding occurs around the first periastron, stops, and then restarts much later in the evolution (visible as a relative drop in the bound mass as compared to the mass that leaves the grid, and most significant for their simulations 4 and 5).

By $t = 13$ d the total change in unbound mass is given by $\Delta M_{\rm unb} \approx 0.22$ M$_\odot$ or about 14% of the envelope mass, and this reduces to 0.21 M$_\odot$ or 13% of the envelope mass between $t \approx 17$ d and $t \approx 19$ d. This is comparable to the fraction of 13% obtained by Iaconi et al. (2017). Using the moving mesh code AREPO with initial conditions very close to ours, Ohlmann et al. (2016) obtained

a value of 8% by the end of their simulation, and found that most of this was ejected during the first 40 d. The difference between their value and ours is likely caused by the slight differences in initial conditions (see App. A for a detailed comparison, and a discussion of differences in the initial conditions).

Although the gas energy $E_{\rm gas}$ hardly changes between $t = 0$ and the end of plunge-in at $t \approx 13$ d (and likewise for E_{1-2} since the two are complementary; see Sec. 3), this is when most of the envelope unbinding occurs. Some of the gas gains energy to become less bound, while the remainder loses energy to become more bound and the net change is nearly zero. This happens as the secondary plunges toward the bulk of material at the centre, strengthening its overall pull on the envelope, but also imparting an impulse to the gas it encounters locally. To understand this in more detail, we discuss the spatial variation of the energy density in Sec. 4.2.

The other lines in Fig. 2 represent changes in unbound mass using alternative definitions of 'unbound'. More liberal definitions plotted are $\mathcal{E}_{\rm gas} - \mathcal{E}_{\rm pot,gas-gas} \geqslant 0$ (exclusion of self-gravity; orange dashed), $\mathcal{E}_{\rm gas} + P \geqslant 0$ (replacement of internal energy density with enthalpy density; red dashed-dotted), and $\mathcal{E}_{\rm gas}^{\rm CM_{1-2}} \geqslant 0$, where the left-hand-side is the gas energy density in the frame of the particles' centre of mass (blue dashed-double-dotted; we motivate this choice in Sec. 5). We also plot $\mathcal{E} - \mathcal{E}_{\rm int,gas} \geqslant 0$ (exclusion of the internal energy density; green dotted) for comparison. For each curve, the unbound mass at $t = 0$, located in the ambient medium, is subtracted from the total unbound mass, as well as any unbound mass that has entered through the domain boundaries.

Ivanova & Nandez (2016) previously argued that energy deposition occurs only outside the orbit of the particles. Although the gas between the particles is not undisturbed as seen in 2D slices of density or energy (Sec. 4.2 and Paper I), the effect on the gas outside the orbit is likely stronger than inside it. In calculating the unbound mass fraction it is then an interesting alternative to exclude the mass of gas within a sphere of radius $a(t)$ centred on particle 1. About 23% of the envelope mass resides within a distance a from particle 1 at $t = 13$ d, dropping to 3% at $t = 40$ d. At both times, most all of this interior mass is bound. Therefore, the change in the unbound mass for the 'exterior' envelope is basically unchanged from the values we calculated for the whole envelope (Fig. 2). The total envelope mass is $1.6\,{\rm M}_\odot$ and at the end of plunge-in at $t = 13$ d, 18% of the envelope mass exterior to the orbit is unbound, compared with 14% of the whole envelope.

4.2 Spatial analysis

To interpret Fig. 2 and the partial unbinding of the envelope, we now explore the time-dependent spatial distribution of energy. We define a normalized energy density $\mathcal{E}_{\rm gas,norm} = \mathcal{E}_{\rm gas}/\max(\mathcal{E}_{\rm bulk,gas} + \mathcal{E}_{\rm int,gas},\ -\mathcal{E}_{\rm pot,gas})$ (where $\mathcal{E}_{\rm pot,gas} = \mathcal{E}_{\rm pot,gas-1} + \mathcal{E}_{\rm pot,gas-2} + \mathcal{E}_{\rm pot,gas-gas}$) and plot snapshots of $\mathcal{E}_{\rm gas,norm}$ in the orbital plane in the top row of Fig. 3 for $t = 5$, 10, 20 and 30 d. For our fiducial definition of unbound, $\mathcal{E}_{\rm gas} \geqslant 0$, blue corresponds to bound material while red corresponds to unbound material, and -1 (1) means maximally bound (unbound). Much of the ambient material is initially unbound due to its large internal energy density and large distance from the central mass concentration. Contours show the gas density while the component of the velocity in the orbital plane is shown with arrows.

The second row of Fig. 3 shows $(\mathcal{E}_{\rm int,gas} - \mathcal{E}_{\rm bulk,gas})/\max(\mathcal{E}_{\rm int,gas}, \mathcal{E}_{\rm bulk,gas})$. Magenta (green) represents gas for which $\mathcal{E}_{\rm int,gas}$ is larger (smaller) than $\mathcal{E}_{\rm bulk,gas}$. These plots correspond closely with similar plots for Mach number; magenta (green) regions correspond to subsonic (supersonic) gas. The third and fourth rows of Fig. 3 show the same quantities as the top two rows, but in a slice through the plane orthogonal to the orbital plane that intersects the particles. Fig. 4 shows a sequence of eight snapshots for each quantity, spaced by ~ 0.9 d, between $t = 12.0$ d and 18.5 d, now zoomed in by a factor of two compared with those of Fig. 3.

During the plunge-in, material is torn away from the envelope by the secondary, forming a tidal bulge that wraps around in a spiral morphology, trailing the secondary in its orbit (density contours). Gas closest to particle 2 in this spiral wake moves supersonically in a direction in between radially outward and tangential to the path of particle 2. The wake contains highly supersonic unbound gas extending from particle 2 (red and green in the topmost and second-from-top rows, respectively), surrounding a bound region (blue and magenta/yellow) trailing particle 2. Where the spiral wake encounters the low density ambient medium, a spiral shock forms. This does not greatly effect the motion of the outward moving unbound gas (see Sec. 4.3) which slows as it climbs out of the potential well.

At $t \approx 11$ d, after roughly the first half-orbital revolution, newly unbound material near particle 2, followed by particle 2 itself and the dense bulge trailing it, violently collide with dense gas in the bulk of the relatively undisturbed RG envelope. This occurs as the inter-particle separation shrinks rapidly from dynamical friction while the secondary, with its near-side tidal bulge in tow, catches up to the tidal bulge of the RG on the far side of the RG from the secondary that lags the particles in their orbit. [2]

From the collision, an almost radial spiral shock forms near the secondary that connects to the primarily azimuthal shock farther out. This can be seen in the top two rows of Fig. 4, showing the evolution of $\mathcal{E}_{\rm gas,norm}$ and $(\mathcal{E}_{\rm int,gas} - \mathcal{E}_{\rm bulk,gas})/\max(\mathcal{E}_{\rm int,gas}, \mathcal{E}_{\rm bulk,gas})$ between 12.0 d and 14.8 d. Note that the velocity of the gas immediately left of the shock (shown by vector arrows) decreases as the shock forms. The shock structure widens in time as more gas gets shocked. Correspondingly, bulk kinetic energy is converted to internal energy at $t \approx 13$ d, consistent with the quantitative evolution of the contributions to the global energy budget shown in Fig. 1.

However, the total energy density $\mathcal{E}_{\rm gas}$ in the central part of the spiral wake near the secondary decreases between $t \approx 13$ d and $t \approx 15$ d, causing unbound material to become bound once again. This is visible in the top part of Fig. 4, where red material near the secondary becomes blue. We can see that at $t \approx 13$ d (termination of plunge-in), the unbound part of the wake "detaches" from the secondary because the secondary no longer supplies enough energy to unbind the material in its immediate surroundings. This material lies deep in the potential well and is surrounded by dense overlying layers that impede its outward motion. The part of the spiral wake that transitions from unbound to bound between $t \approx 13$ d and $t \approx 15$ d explains the peak and subsequent dip in total unbound mass in Fig. 2 at $t \approx 13$ d (blue solid curve).

The subsequent rise in the unbound mass starting at $t \approx 15$ d and lasting for a few days can be explained with reference to the bottom row of Fig. 4, which shows the time frame $t = 15.7$ d to $t = 18.5$ d. At this time (about 1.5 orbital revolutions after the start of the simulation) the shocked spiral structure trailing the secondary moves at an angle $< 90°$ with respect to the far-side tidal bulge gas, and their relative velocity is much smaller than when they first

[2] MacLeod et al. (2018b,a) see a similar morphology at a comparable stage in their simulations, which have more realistic initial conditions than our own.

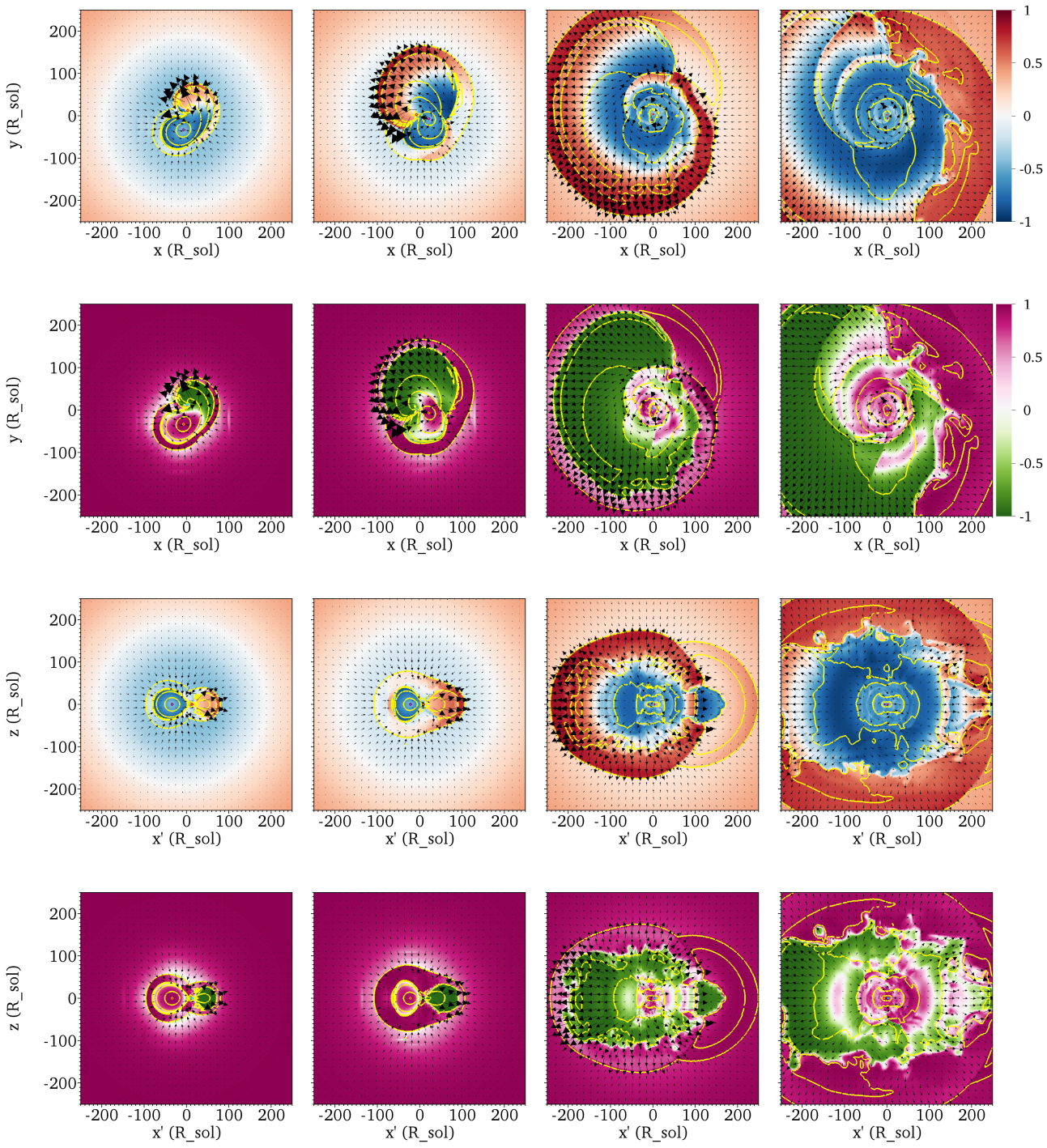

Figure 3. *Top row:* Snapshots of the quantity $\mathcal{E}_{\rm gas}/\max(\mathcal{E}_{\rm bulk,\,gas} + \mathcal{E}_{\rm int,\,gas}, -\mathcal{E}_{\rm pot,\,gas})$, where $\mathcal{E}_{\rm pot,\,gas} = \mathcal{E}_{\rm pot,\,gas-1} + \mathcal{E}_{\rm pot,\,gas-2} + \mathcal{E}_{\rm pot,\,gas-gas}$, in the orbital plane at $t = 5$, 10, 20 and 30 d. At $t = 0$, both particles are situated on the x-axis with particle 2 (circular red contour near centre) located to the right of particle 1 (circular mauve contour near centre), and the orbit is anti-clockwise. A value of 1 corresponds to a maximally unbound system, while a value of -1 corresponds to a maximally bound system, for our standard definition of 'unbound': $\mathcal{E}_{\rm gas} \geqslant 0$. Yellow contours show the density from $\rho = 10^{-4}\,{\rm g\,cm^{-3}}$ downward in logarithmic intervals of 1 dex. Vectors show the component of the velocity parallel to the orbital plane (representing the points located at the ends of the arrow tails). The frame of reference is that of the simulation, and each plot is centred on the particle centre of mass. *Second row from top:* As for the top row but now showing the quantity $(\mathcal{E}_{\rm int,\,gas} - \mathcal{E}_{\rm bulk,\,gas})/\max(\mathcal{E}_{\rm int,\,gas}, \mathcal{E}_{\rm bulk,\,gas})$. This compares the internal and bulk kinetic energy densities. Magenta means internal energy dominates (between the two forms), green means bulk kinetic energy dominates, and white means they are approximately equal. Softening spheres are now represented by orange and cyan contours for particles 1 and 2, respectively. *Second row from bottom:* As top row but now for the plane orthogonal to the orbital plane intersecting both particles. *Bottom row:* As second row from top but now for the plane orthogonal to the orbital plane intersecting both particles.

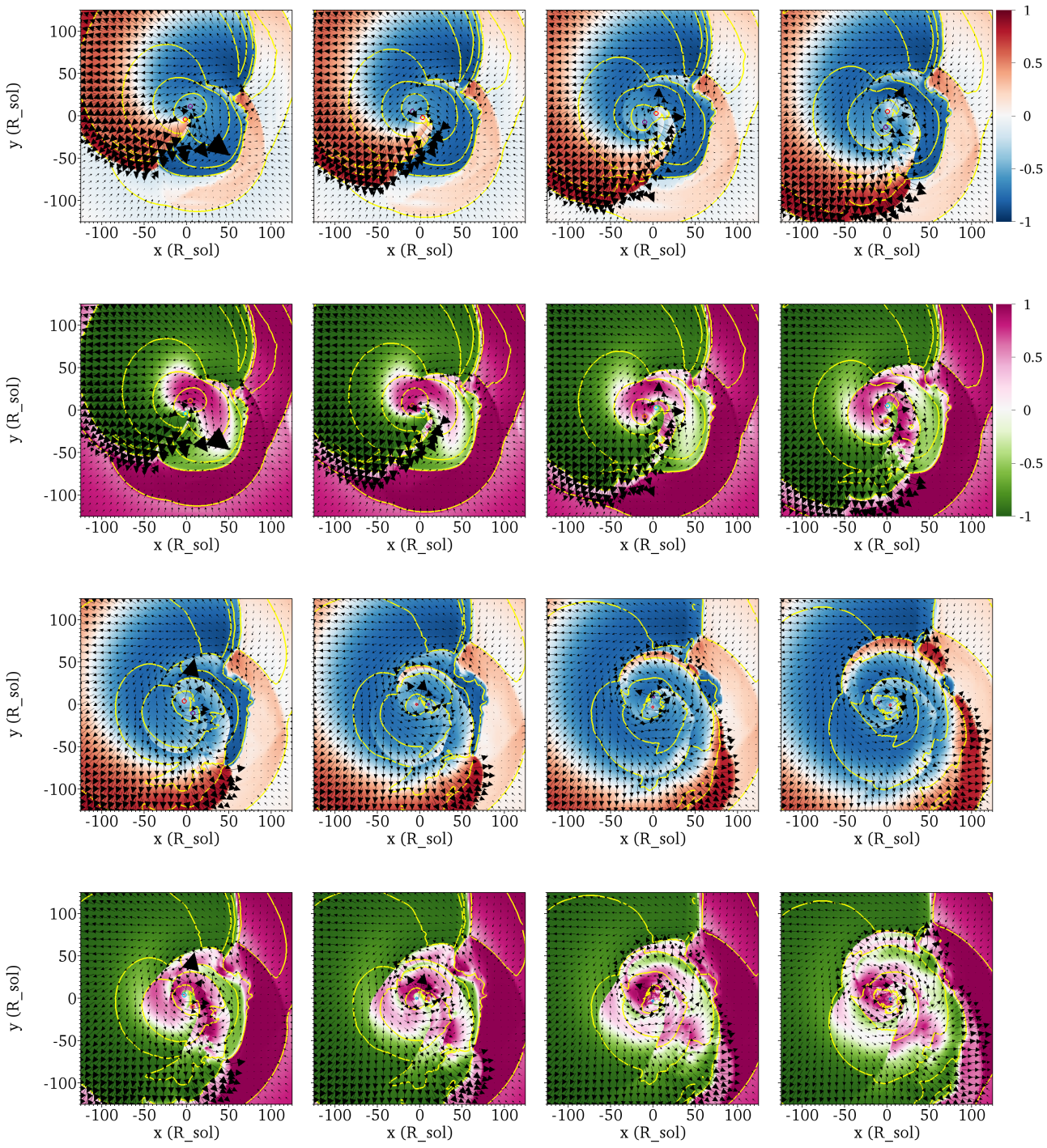

Figure 4. Similar to the top two rows of Fig. 3 but zoomed in and showing eight snapshots equally spaced in time (by about 0.9 d) between $t = 12.0$ d and $t = 18.5$ d. Particles complete only a fraction of an orbital revolution between successive snapshots. In the top row, showing $t = 12.0$ d to $t = 14.8$ d, the most recently energized unbound material (red, near particle 2) becomes bound (blue) when it loses kinetic energy as it collides with the bulk of the envelope material. In the second-from-bottom row, showing $t = 15.7$ d to $t = 18.5$ d, some of the bound material in the spiral wake of particle 2 becomes unbound (above centre) as it moves into a lower density region.

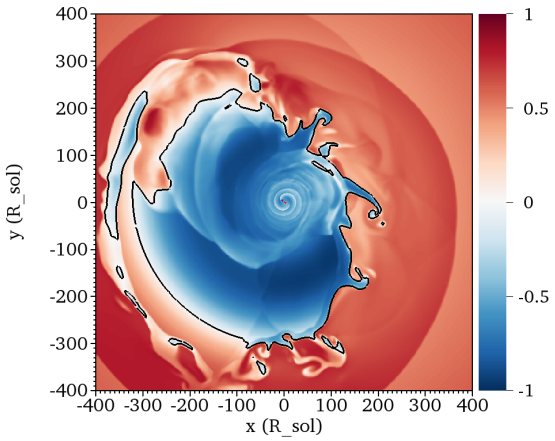

Figure 5. caption The normalized gas energy $\mathcal{E}_{\rm gas,norm}$ with blue (red) showing bound (unbound) gas at $t = 40$ d, with contours delineating the value zero. Recently formed islands of bound gas are seen near the envelope-ambient interface, showing how unbound envelope gas can become bound as it transfers energy to the ambient medium. The CM of the particles is at (0,0) and the primary and secondary particle softening spheres are represented by mauve and red contours, respectively (near centre, barely visible due to the scale of the plot).

collided. The inertia of the dense spiral wake and the negative pressure gradient (nearly aligned to the density gradient) allow the wake to accelerate up to a nearly constant speed toward larger y. This happens in spite of the work done by gravity so the overall energy density of the wake increases.

This process repeats during the next orbital revolution, resulting in a third layer of unbound gas that can be seen as the innermost strip of red on the upper-left of the rightmost panel in the top row of Fig. 3 at $t = 30$ d. By this time, a separate spiral wake trails behind particle 1, but this wake does not gain enough energy as it moves outward to become unbound. In subsequent orbital revolutions, a smaller amount of material transitions from bound to unbound, now toward positive x; an example is visible in the same panel at $t = 30$ d (right of centre in the plot). In this snapshot, Rayleigh-Taylor (RT) instability-produced "fingers" are visible at large distances from the centre. Such features are formed as the outward-moving interface between inner dense gas and outer diffuse gas decelerates.

After $t \approx 19$ d, pockets of gas can be seen to transition from unbound to bound near the edge of the expanding envelope. This is most obvious late in the simulation. In Fig. 5 we show a snapshot at $t = 40$ d. In addition to the RT fingers of bound material mentioned above, recently formed isolated blue "islands" of bound material are visible.

4.3 Efficiency of partial envelope removal

Since unbound material will never have exactly zero energy density, there is always an efficiency associated with the energy transfer process. To get an idea about how much energy is "wasted" by increasing the energy density of already unbound material, we plot various energy components with time for gas that is *unbound* in the bottom panel of Fig. 1. From the orange line, we see that during the simulation a net amount of about 0.2×10^{47} erg of energy is gained by the unbound gas. As the change in gas energy during the simulation is 1.3×10^{47} erg, the fraction that ends up in unbound gas is about 15%. This gives us an estimate of how much of the particle energy is wasted.

How does the energy transfer to unbound material take place and what happens subsequently? We see from the bottom panel of Fig. 1 that most of the increase in energy of the unbound material occurs in the first 13 d. This is consistent with the change in the unbound mass $\Delta M_{\rm unb}$ also peaking at $t \approx 13$ d. The energy transferred is mainly in the form of kinetic energy, as material is launched outward during plunge-in. Subsequently, the unbound gas, whose mass remains almost constant after $t = 13$ d, sees much of its bulk kinetic energy get converted to internal energy and potential energy.

There is another way in which energy transfer to the envelope is inefficient. To expand, the envelope must displace ambient material, which has significant pressure and mass in our simulation. Work must be done by the envelope against thermal pressure of the ambient material, ram pressure as the envelope expands into ambient gas, and also to displace ambient material against gravity. These terms can respectively be estimated as $\sim (4\pi/3)P_{\rm amb}r_{\rm f}^3$, $\sim (4\pi/3)\rho_{\rm amb}v_r^2 r_{\rm f}^3$ and $\sim (4\pi/3){\rm G}r_{\rm f}^2(M_1+M_2)\rho_{\rm amb}$, where $P_{\rm amb} = 1 \times 10^5$ dyn cm^{-2} is the ambient pressure, $\rho_{\rm amb} = 7 \times 10^{-9}$ g cm^{-3} is the ambient density, $M_1 = 2\,{\rm M}_\odot$ is the primary mass, $M_2 = 1\,{\rm M}_\odot$ is the secondary mass, $r_{\rm f} \sim 3 \times 10^{13}$ cm is the radius of the envelope at $t = 40$ d, and $v_r \sim 40$ km s^{-1} is a typical speed at which the envelope expands into the surroundings. With these expressions we obtain $\sim 0.1 \times 10^{47}$ erg for each work term. Thus, $\sim 0.3 \times 10^{47}$ erg may have been transferred from the envelope to the ambient medium during the course of the simulation. This is a small amount compared to the total envelope energy, but indicates that the expansion of the envelope would have been slightly faster within a less dense or lower pressure ambient medium. It also explains the decrease in unbound mass after $t \approx 19$ d. A circumbinary torus is likely to remain from the RLOF stage preceding CEE, and this material would shape the envelope and redirect its expansion (MacLeod et al. 2018a; Reichardt et al. 2018).

4.4 Timescale for ejecting the envelope and final separation

The average rate of energy transfer from the particles to the gas is approximately constant at the end of the simulation, and equal to about 0.03×10^{47} erg d^{-1} (final average slope of orange curve of top panel of Fig. 1). Of this transfer rate, about 0.001×10^{47} erg d^{-1}, a negligible fraction, is being transferred from the particles to gas that is already unbound (final slope of orange curve of bottom panel of Fig. 1). Thus, although the envelope continues to gain energy at a relatively high rate, this energy is being gained by material that is still bound by the end of the simulation. Assuming that this energy transfer rate of 0.03×10^{47} erg d^{-1} remains constant, one can estimate how long it would take for the gas to attain zero total energy, and we find it would take an additional 38 d. However, this calculation uses the total gas energy, which includes the energy of the ambient medium, equal to $E_{\rm amb} \sim 0.5 \times 10^{47}$ erg. Thus, to obtain a more accurate estimate, we subtract this ambient energy from the value of $E_{\rm gas}$ at $t = 40$ d given in Tab. 1, which gives an envelope gas energy of $E_{\rm e} \sim -1.65 \times 10^{47}$ erg. Then the additional time needed for the envelope to attain $E_{\rm gas} = 0$ would be about 55 d after the end of the simulation at $t = 40$ d.

Now, from Sec. 4.3 we know that not all of the liberated particle orbital energy will be transferred to bound material, and that this leads to an efficiency factor ϵ, found to be about 85% in the first 40 d (that is, 15% of the energy gets wasted). Assuming an efficiency of $\epsilon = 0.85$ for the remainder of the evolution, the time calculated above must be divided by ϵ, giving ~ 65 d. As the system continues

to evolve, less and less gas would remain bound, so we would expect that more of the released orbital energy would go into unbound gas, resulting in reduced efficiency. With an efficiency of only 10%, the released orbital energy would have to be about 16.5×10^{47} erg, and the timescale for ejecting the envelope would be ~ 550 d, or about 1.5 yr, which is small enough to be consistent with observations of post-CE binary systems, for which the envelope has already been ejected. In Ohlmann et al. (2016), the orbital energy decay rate of the particles decreases to become much smaller by the end of their simulation at $t \sim 130$ d than at $t = 40$ d. The assumption that this decay rate remains constant is therefore probably too optimistic.

The orbital energy of the particles at $t = 40$ d is about $E_{1-2}(40\,\mathrm{d}) = -0.95 \times 10^{47}$ erg (Tab. 1). Then, equating the gas energy with the difference in particle energy between $t = 40$ d and envelope ejection, multiplied by the efficiency ϵ, we derive the following expression for the final separation:

$$a_\mathrm{f} \sim \frac{\mathrm{G}M_{1,\mathrm{c}}M_2}{2}\left(\frac{E_\mathrm{amb} - E_\mathrm{gas}(40\,\mathrm{d})}{\epsilon} - E_{1-2}(40\,\mathrm{d})\right)^{-1}. \quad (1)$$

This estimate is independent of the rate of energy transfer (and foreshadows our discussion of the CE EF in Sec. 6). Putting $\epsilon = 1$ gives the upper limit $a_\mathrm{f} \sim 2.9\,\mathrm{R}_\odot$, while for $\epsilon = 0.85$ we obtain $a_\mathrm{f} \sim 2.6\,\mathrm{R}_\odot$ and for $\epsilon = 0.1$ we obtain $a_\mathrm{f} \sim 0.4\,\mathrm{R}_\odot$.

5 PARTICLE CENTRE OF MASS MOTION AND PLANETARY NEBULA–CENTRAL STAR OFFSETS

The asymmetry of the gas distribution in the orbital plane rapidly evolves, moving the particle and gas centres of mass (CM) oppositely in the simulation frame, while nearly conserving linear momentum (see also Sandquist et al. 1998; Ohlmann et al. 2016). The top panel of Fig. 6, shows the paths in the orbital plane traced by the particle CM (blue), gas CM (red), and system CM (green). The system CM position remains relatively fixed with small speed ($< 0.2\,\mathrm{km\,s^{-1}}$); deviations in its position are caused by small errors in linear momentum conservation.

The bottom panel of Fig. 6 shows the speed of the particle CM versus time in blue, that of the gas CM in red, and that of the system CM in green. Until the end of the plunge-in phase at $t \approx 13$ d, the relative speed between the gas CM and particle CM, obtained by adding the red and blue curves, is 53-71 $\mathrm{km\,s^{-1}}$, and the final relative speed is 5 to 6 $\mathrm{km\,s^{-1}}$. Sandquist et al. (1998) found the speed of the particle CM relative to the system CM frame at the late stages of CEE to be 3 $\mathrm{km\,s^{-1}}$, for their simulation of a 3 $\mathrm{M}_\odot$ AGB star with 0.4 $\mathrm{M}_\odot$ companion.

Our standard definition of 'unbound,' $\mathcal{E}_\mathrm{gas} \geqslant 0$, does not account for relative motion of the particle binary system CM and that of the disrupted envelope gas. The particles' kinetic energy and bulk kinetic energy of the gas are given in the inertial frame of the simulation, which is the system CM frame if small deviations from linear momentum conservation are neglected. To account for the relative CM motion while neglecting non-inertial effects in the frame of the particle CM, the bulk kinetic energy of gas would be $E^{\mathrm{CM}_{1-2}}_{\mathrm{bulk,gas}} = \frac{1}{2}\int \rho(\boldsymbol{x})|\boldsymbol{v}(\boldsymbol{x}) - \boldsymbol{v}^{\mathrm{CM}_{1-2}}|^2 \mathrm{d}V$. This refined definition implies that gas moving faster (slower) with respect to the particle CM than the system CM is more (less) unbound than for the standard definition. As seen in Fig. 2, the change in unbound mass using this modified definition (dashed-double-dotted blue) has a higher maximum but lower final value than the standard definition (solid blue). The opposite motion of the envelope CM and particle CM leads to an increase in the total mass of unbound gas at early times. However, the particles eventually carry their own individual gas "envelopes" (Paper I), which likely explains the reduction in the unbound mass seen at late times.

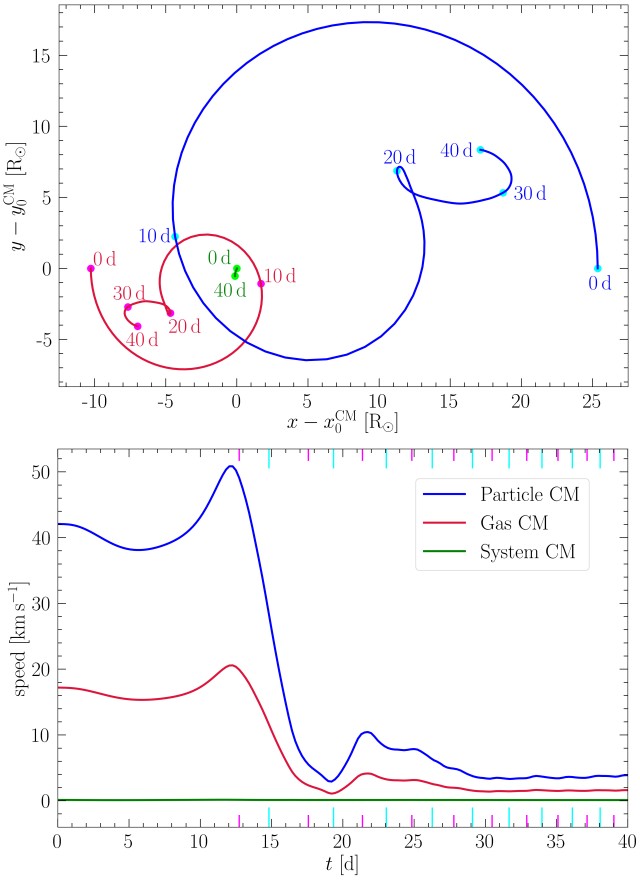

Figure 6. *Top:* Motion in orbital plane of the particle CM (blue), gas CM (red) and net system CM (green). The system CM moves slowly and gradually downward in the plot during the course of the simulation. *Bottom:* Evolution of the speed relative to the reference frame in which the simulation is carried out, for the particle CM (blue), gas CM (red) and net system CM (green).

5.1 PN central star offsets

Several bipolar PNe exhibit an offset between the binary central star and PN centre (e.g. MyCn 18: Sahai et al. 1999; Clyne et al. 2014; Miszalski et al. 2018; Hen 2-161: Jones et al. 2015; Abell 41: Jones et al. 2010), and the Etched Hourglass Nebula MyCn 18 is the best studied among them. Previous attempts to explain the offset have failed (Miszalski et al. 2018, and references therein).

The observed distance to MyCn 18 is 618 ± 101 au (Miszalski et al. 2018) and the estimated time since the end of the CE phase is ~ 2700 yr (Clyne et al. 2014; Miszalski et al. 2018). This requires a mean relative velocity of $\sim 1\,\mathrm{km\,s^{-1}}$ between the PN central star and nebula in the plane of the sky to explain the offset if the motion started at the end of the CE phase. The speeds of $\sim$ 4-6 $\mathrm{km\,s^{-1}}$ that we obtain for the particle CM relative to the inertial frame and envelope CM are of the required order of magnitude at the end of our simulation. The direction of the observed offset is within 5° of the PN minor axis, and likely parallel to the orbital plane of the binary (Hillwig et al. 2016). This agrees with the motion of the particle CM in our simulation, whose velocity in the z-direction perpendicular to the orbital plane has magnitude $\leqslant 0.3\,\mathrm{km\,s^{-1}}$ during the simulation,

with average z-velocity only $-6 \times 10^{-3}\,\mathrm{km\,s^{-1}}$ between $t = 30\,\mathrm{d}$ and $t = 40\,\mathrm{d}$.

For the MyCn 18 system, Miszalski et al. 2018 obtain primary and secondary masses of $0.6 \pm 0.1\,\mathrm{M_\odot}$ and $0.19 \pm 0.05\,\mathrm{M_\odot}$ respectively, whereas our particle masses are $M_{1,\mathrm{c}} = 0.4\,\mathrm{M_\odot}$ and $M_2 = 1\,\mathrm{M_\odot}$. Observations provide only a plane-of-the-sky projection, and thus a minimum of the full 3D offset, which would require a larger offset velocity.

More realistic simulation initial conditions–such as those which start from the RLOF–may result in somewhat more symmetric mass ejection (Reichardt et al. 2018) and hence somewhat smaller relative CM speeds than we find. Nevertheless, because the relative motion between the particle CM and envelope seen in our simulation is consistent with observations, our proposed mechanism for such offsets warrants further study.

6 ENERGY FORMALISM

6.1 Old vs. new α_{CE} prescriptions

A common approach for quantifying envelope unbinding in CEE is the so called "energy formalism" (EF). As expressed in Eq. 3 of Ivanova et al. (2013), this is

$$\frac{\mathrm{G}M_1 M_{1,\mathrm{e}}}{\lambda R_1} = \alpha_{\mathrm{CE}} \frac{\mathrm{G}M_2}{2} \left(\frac{M_{1,\mathrm{c}}}{a_\mathrm{f}} - \frac{M_1}{a_\mathrm{i}} \right) \tag{2}$$

where $M_{1,\mathrm{e}} = M_1 - M_{1,\mathrm{c}}$, the quantities α_{CE} and λ are parameters, a_i and a_f are the initial and final orbital radial. The formula applies only when 'final' refers to the time at which the envelope becomes completely unbound such that drag is eliminated and the inspiral halts. The left-hand-side (LHS) is the envelope 'binding energy,' which includes the *negative* of the potential energy due to the gas–particle 1 gravitational interaction as well as that due to gas self-gravity. The parameter λ can be calculated from first principles for a known envelope density profile.[3] Following convention, the'binding energy' also includes the negative of the envelope internal energy, so the equation of state must also be known to compute λ. The right-hand-side (RHS) of equation (2) is the energy used to unbind envelope gas, and equals the negative of the change in the orbital energy of the system between $t = t_\mathrm{i}$, when $a = a_\mathrm{i}$, and $t = t_\mathrm{f}$, when $a = a_\mathrm{f}$, multiplied by an efficiency factor α_{CE}. The value of α_{CE} estimated from population synthesis studies is $0.1 \leqslant \alpha_{\mathrm{CE}} \leqslant 0.3$ (Davis et al. 2010; Zorotovic et al. 2010; Cojocaru et al. 2017; Briggs et al. 2018), though it is still largely unknown and could also vary between different types of objects.

We now propose an alternative to equation (2) that has all terms contributing to E_{gas} on the LHS, and all terms contributing to E_{1-2} on the RHS. Specifically,

$$\mathrm{G}M_{1,\mathrm{e}} \left[\frac{M_1}{\lambda R_1} + \frac{M_2}{2a_\mathrm{i}} \left(1 + \frac{M_1}{M_1 + M_2} \right) \right] = \widetilde{\alpha}_{\mathrm{CE}} \frac{\mathrm{G}M_2}{2} \left\{ \frac{M_{1,\mathrm{c}}}{a_\mathrm{f}} - \frac{M_1}{a_\mathrm{i}} \left[\frac{M_{1,\mathrm{c}}}{M_1} - \left(1 - \frac{M_{1,\mathrm{c}}}{M_1} \right) \frac{M_1}{M_1 + M_2} \right] \right\}. \tag{3}$$

Equation (3) makes use of the relations $v_1^2 = \mathrm{G}\mu M_2/(aM_1)$ and $v_2^2 = \mathrm{G}\mu M_1/(aM_2)$ for circular orbit speeds in the inertial CM frame in the standard two-body problem, with reduced mass $\mu \equiv M_1 M_2/(M_1 + M_2)$. Details are provided in App. B, where we also present an alternative form of the equation. Equation (3) differs from equation (2) in that the initial orbital energy involving the envelope and particle 2 is now on the LHS, and not multiplying $\widetilde{\alpha}_{\mathrm{CE}}$. As a result, equations (2) and (3) are equivalent if and only if $\alpha_{\mathrm{CE}} = \widetilde{\alpha}_{\mathrm{CE}} = 1$. Equation (3) tells us how particle energy has been converted with an efficiency $\widetilde{\alpha}_{\mathrm{CE}}$ into gas energy during the envelope unbinding process. This is similar to the approach in Sec. 4.4, with $\widetilde{\alpha}_{\mathrm{CE}}$ replacing ϵ.

Equation (3) appears lengthy compared to equation (2), but overcomes a conceptual deficiency of the latter. In equation (3), we include the contribution $E_{\mathrm{bulk,gas,i}} + E_{\mathrm{pot,gas-2,i}} < 0$ in the negative binding energy of the envelope, not in terms multiplying $\tilde{\alpha}_{\mathrm{CE}}$, contrasting what multiplies α_{CE} in equation (2). If energy from the envelope is redistributed therein to allow more total unbound gas even without extra energy sources or sinks, then it can awkwardly lead to $\alpha_{\mathrm{CE}} > 1$, muddling the physical interpretation of α_{CE} . In contrast, our new form of equation (3) guarantees $\widetilde{\alpha}_{\mathrm{CE}} \leqslant 1$.

Equation (2) or (3) can be inverted to give an expression for a_f. In the limit $\alpha_{\mathrm{CE}} \ll 1$, equation (2) leads to $a_\mathrm{f} \sim (\alpha_{\mathrm{CE}}\lambda/2)(M_{1,\mathrm{c}}/M_1)(M_2/M_1)(1 - M_{1,\mathrm{c}}/M_1)^{-1} R_1 \equiv X(\alpha)$, while in the limit $\widetilde{\alpha}_{\mathrm{CE}} \ll 1$, equation (3) leads to $a_\mathrm{f} \sim [1 + (\lambda/2)(R_1/a_\mathrm{i})(M_2/M_1)]^{-1} X(\widetilde{\alpha})$. These asymptotic expressions produce larger values than equations (2) and (3) by only $\sim 10\%$ for $\alpha = 0.25$ or $\widetilde{\alpha} = 0.25$ and the other choices of parameter ranges used in this work, and are convenient for estimating how a_f depends on various parameters, although we use the full expressions to obtain numerical values.

6.2 Applying the energy formalism

Equations (2) and (3) only apply if a_f corresponds to the inter-particle separation after the envelope is completely unbound. Since this is *not* the case at $t = t_\mathrm{f}$ in the simulation, we cannot use the simulation data to obtain α_{CE} or $\widetilde{\alpha}_{\mathrm{CE}}$, respectively, but we can check whether we should *expect* the envelope to be unbound at $a = 7\,\mathrm{R_\odot}$, given a reasonable estimate for α_{CE} or $\widetilde{\alpha}_{\mathrm{CE}}$.

To assess the consistency between simulation results and theoretical expectations, we evaluated the various energy terms of Tab. 1 at $t = 0$ for the envelope alone, excluding the ambient medium. The values are listed in the fourth column of Tab. 2. We have verified that small differences between a value from Tab. 2 and the corresponding value in the fourth column of Tab. 1, is accounted for by energy in the ambient medium.

We next evaluate the left and right sides of equations (2) and (3), for $a_\mathrm{i} = 49\,\mathrm{R_\odot}$ and $a_\mathrm{f} = 7\,\mathrm{R_\odot}$, which is the approximate mean inter-particle separation at $t = 40\,\mathrm{d}$. For the RG in our model, λ evaluates to 1.31. The first and third rows of Tab. 3 respectively show the LHS and RHS of equations (2) and (3) for the simulation. For the LHS and RHS to be equal, $2 \leqslant \widetilde{\alpha}_{\mathrm{CE}}, \alpha_{\mathrm{CE}} \leqslant 5$ would be required. Since $\widetilde{\alpha}_{\mathrm{CE}} > 1$ is unphysical, we should *not expect* the envelope to be unbound at $a = 7\,\mathrm{R_\odot}$, in agreement with the simulation results.

Realistically, the initial state at $t = t_\mathrm{i}$ might be the RLOF stage, just prior to CEE (MacLeod et al. 2018b). This would imply a larger value of a_i, and smaller contributions from the terms ($\propto 1/a_\mathrm{i}$) that differ between equations (2) and (3). We can estimate the orbital separation in the RLOF phase as the Roche-lobe radius (Eggleton 1983),

$$r_\mathrm{L} = \frac{0.49 q^{2/3} a}{0.6 q^{2/3} + \ln(1 + q^{1/3})}. \tag{4}$$

For the system studied in this work $q = M_1/M_2 = 2$, and this gives

[3] Alternatively, λ can be combined with α_{CE}, resulting in a single parameter $\lambda\alpha_{\mathrm{CE}}$.

Table 2. Similar to Tab. 1, but now showing the initial energy, in units of 10^{47} erg, for the initial condition of the simulation (RGB primary with $a_\mathrm{i} = 49\,\mathrm{R}_\odot$, fourth column from left) as well as for three other initial conditions involving the same secondary but a different initial separation and/or an AGB, rather than RGB, primary (columns 5-7). Unlike for Tab. 1, values do not include the contribution of the ambient medium.

			Red giant		Asymptotic giant	
Energy component at $t = 0$	Symbol	Expression	$a_\mathrm{i} = 49\,\mathrm{R}_\odot$	$a_\mathrm{i} = 109\,\mathrm{R}_\odot$	$a_\mathrm{i} = 124\,\mathrm{R}_\odot$	$a_\mathrm{i} = 284\,\mathrm{R}_\odot$
Particle 1 kinetic	$E_{\mathrm{bulk,1,i}}$	$\frac{1}{2}M_{1,\mathrm{c}}v_{1,\mathrm{c}}^2$	0.05	0.02	0.03	0.01
Particle 2 kinetic	$E_{\mathrm{bulk,2,i}}$	$\frac{1}{2}M_2 v_2^2$	0.49	0.22	0.17	0.07
Particle-particle potential	$E_{\mathrm{pot,1-2,i}}$	$-\mathrm{G}M_{1,\mathrm{c}}M_2/a$	−0.28	−0.12	−0.16	−0.07
Envelope bulk kinetic	$E_{\mathrm{bulk,e,i}}$	$\frac{1}{2}m_\mathrm{e}v_{1,\mathrm{i}}^2$	0.20	0.09	0.07	0.03
Envelope internal	$E_{\mathrm{int,e,i}}$	$4\pi\int_0^{R_1}\frac{P}{\gamma-1}r^2dr$	1.81	1.81	0.71	0.71
Envelope-envelope potential	$E_{\mathrm{pot,e-e,i}}$	$-(4\pi)^2\mathrm{G}\int_0^{R_1}\rho(r)r\int_0^r\rho(r')r'^2dr'dr$	−2.13	−2.13	−0.57	−0.57
Envelope-particle 1 potential	$E_{\mathrm{pot,e-1,i}}$	$-4\pi\mathrm{G}m_{1,\mathrm{c}}\int_0^{R_1}\rho r dr$	−1.56	−1.56	−0.88	−0.88
Envelope-particle 2 potential	$E_{\mathrm{pot,e-2,i}}$	$-\frac{\mathrm{G}m_2m_\mathrm{e}}{a_\mathrm{i}}$	−1.20	−0.54	−0.37	−0.16
Particle total	$E_{1-2,\mathrm{i}}$	$E_{\mathrm{bulk,1,i}}+E_{\mathrm{bulk,2,i}}+E_{\mathrm{pot,1-2,i}}$	0.26	0.12	0.04	0.02
Envelope total	$E_{\mathrm{e,i}}$	$E_{\mathrm{bulk,e,i}}+E_{\mathrm{int,e,i}}+\sum_j E_{\mathrm{e-j,i}}$	−2.87	−2.32	−1.05	−0.88
Total particle and envelope	$E_{1-2-\mathrm{e,i}}$	$E_{1-2,\mathrm{i}}+E_{\mathrm{e,i}}$	−2.61	−2.21	−1.01	−0.86

Table 3. The left and right sides of the EF, given by equation (2) from Ivanova et al. (2013) or equation (3) (this work), for the case where the final inter-particle separation a_f is equal to the mean orbital separation $\approx 7\,\mathrm{R}_\odot$ at the end of the simulation at $t = 40\,\mathrm{d}$, and for different assumptions about the initial separation a_i. The envelope is predicted to be fully unbound when the left-hand and right-hand sides become equal. Examination of the entries leads directly to the conclusion that the envelope is not expected to be unbound at $a = 7\,\mathrm{R}_\odot$, since this would require $\widetilde{\alpha}_\mathrm{CE} > 1$, which is not physical.

	a_i [$\mathrm{R}_\odot$]	LHS [10^{47} erg]	RHS($a_\mathrm{f} = 7\,\mathrm{R}_\odot$) [$10^{47}$ erg]
Eq. (2)	49	1.9	$0.2\alpha_\mathrm{CE}$
Eq. (2)	109	1.9	$0.6\alpha_\mathrm{CE}$
Eq. (3)	49	2.9	$1.2\widetilde{\alpha}_\mathrm{CE}$
Eq. (3)	109	2.3	$1.1\widetilde{\alpha}_\mathrm{CE}$

Table 4. Final inter-particle separations a_f predicted by the EF (2) (Ivanova et al. 2013) or (3) (this work) for various assumed values of α_CE or $\widetilde{\alpha}_\mathrm{CE}$. Initial conditions involving an RGB or AGB primary, with initial separation a_i either slightly greater than the primary radius or equal to the Roche limit separation, are considered. Note that equation (2) contains α_CE, while equation (3) contains $\widetilde{\alpha}_\mathrm{CE}$.

		α_CE or $\widetilde{\alpha}_\mathrm{CE}$:	0.1	0.25	0.5	1
		a_i ($\mathrm{R}_\odot$)	a_f ($\mathrm{R}_\odot$)			
RGB	Eq. (2)	49	0.3	0.8	1.5	2.6
$\lambda = 1.31$		109	0.4	0.9	1.7	3.1
	Eq. (3)	49	0.2	0.6	1.2	2.6
		109	0.3	0.7	1.5	3.1
AGB	Eq. (2)	124	1.3	3.0	5.6	9.8
$\lambda = 0.91$		284	1.3	3.2	6.2	11.5
	Eq. (3)	124	0.9	2.4	4.8	9.8
		284	1.1	2.8	5.7	11.5

$a_\mathrm{i} \approx 109 R_\odot$, which would reduce a_i-dependent terms by more than a factor of two.

Values of the initial energy terms for $a_\mathrm{i} = 109\,\mathrm{R}_\odot$ are given in the fifth column of Tab. 2. The second and fourth rows of Tab. 3, show the LHS and RHS equations (2) and (3) for this larger initial separation. Increasing the initial separation somewhat increases the orbital energy that can be tapped thereby reducing α_CE or $\widetilde{\alpha}_\mathrm{CE}$, but the difference from the case where $a_\mathrm{i} = 49\,\mathrm{R}_\odot$ is small, and $\widetilde{\alpha}_\mathrm{CE} > 1$ would still be required. Failure to unbind the envelope at $a = a_\mathrm{f} \approx 7\,\mathrm{R}_\odot$ is not simply overcome by starting with $a = a_\mathrm{i} = 109\,\mathrm{R}_\odot$ instead of $49\,\mathrm{R}_\odot$. Instead, envelope unbinding requires the binary to tighten to separation $a \ll 7\,\mathrm{R}_\odot$ in the absence of other energy sources.

6.3 Predicting the final inter-particle separation

To predict a_f for a given value of α_CE or $\widetilde{\alpha}_\mathrm{CE}$. We can use equation (2) or equation (3), with either $a_\mathrm{i} = 49\,\mathrm{R}_\odot$ (simulation) or $a_\mathrm{i} = 109\,\mathrm{R}_\odot$ (Roche limit). The values are given in the top half of Tab. 4 for $0.1 \leqslant \alpha_\mathrm{CE} \leqslant 0,5$, and for $\alpha_\mathrm{CE} = 1$ or $\widetilde{\alpha}_\mathrm{CE} = 1$. Tab. 4 tells us that we cannot expect envelope ejection until a has reduced to less than $3\,\mathrm{R}_\odot$, and likely less than $1\,\mathrm{R}_\odot$. This is much smaller than the final separation in our simulation and that of Ohlmann et al. (2016), who used very similar initial conditions but evolved the system to $t \sim 130\,\mathrm{d}$, at which time $a \approx 4\,\mathrm{R}_\odot$. It is therefore consistent with the theory, that the envelope did not eject in the simulation of Ohlmann et al. (2016) either.

The predictions from Tab. 4 are consistent with those of Sec. 4.4, where we obtained $a_\mathrm{f} = 2.9\,\mathrm{R}_\odot$ and $0.4\,\mathrm{R}_\odot$ for $\epsilon = 1$ and 0.1, respectively (recall that $\epsilon \equiv \alpha_\mathrm{CE}$ in equation 3), whereas from Tab. 4, equation (3) gives $a_\mathrm{f} = 2.6$ and 0.2 for $\widetilde{\alpha}_\mathrm{CE} = 1$ and 0.1, respectively. These small differences are caused by the slight differences in the methods (see Sec. 4.4).

This analysis shows that envelope ejection requires the binary separation to reduce further. This possibility was considered in Sec. 4.4, where it was pointed out that even at the end of the simulation at $t = 40\,\mathrm{d}$, energy was being transferred from particles to gas at an almost steady average rate (see Fig. 1), and that if this were to continue to late times, the envelope might be ejected by $\sim 10^2$–$10^3\,\mathrm{d}$, still small enough to account for observations of PPNe, which have ages $> 10^2\,\mathrm{yr}$. The orbital separation does *appear*, from Fig. 1 of Ohlmann et al. (2016), to be approaching

an asymptotic value, while the energy transfer rate reduces with time (their Fig. 2). Therefore, running the simulation longer might not lead to envelope unbinding. They estimate that it would take ~ 100 yr to eject the envelope if unbinding were to continue at the final rate.

Clayton et al. (2017), using idealized 1D MESA CEE simulations which include radiative transport and shock capture, argue that envelopes can be ejected on timescales of $\sim 10^3$ yr. In their models, pulsations develop, some of which lead to the dynamical ejection of shells containing up to $\sim 10\%$ of the envelope mass. Whether these long ejection timescales are in tension with observations is presently uncertain. In general, it is important to assess what other additional physics could be included that would better facilitate envelope ejection.

7 LIMITATIONS OF SIMULATIONS AND IMPLICATIONS FOR ENVELOPE UNBINDING

In our simulation, and likely in others as well, the ambient density and pressure are not negligible and this causes the ambient medium to act as an energy sink (Sec. 4.3). In nature, for example, the expanding envelope would collide with the circumbinary torus left over from the RLOF phase. The envelope could in principle be ejected from the vicinity of the particles, but lose energy from interaction with the environment, and later fall back. The orbital evolution of the particles is therefore also influenced by the ambient medium, which is not accurately captured by the EF.

Simulations have not yet produced unbound envelopes without an additional energy source, namely recombination energy (Nandez et al. 2015; Nandez & Ivanova 2016; Ivanova & Nandez 2016). Without recombination energy, the envelope is typically unbound at a level of only $\sim 10\%$ of its mass by the end of the simulation (see Iaconi et al. 2017, for a review of CE simulations). Incorporation of the recombination energy was implemented using a subgrid prescription that assumes that the latent energy released by recombination is absorbed locally, and does not account for any transport of energy by radiation or convection. Debate over whether this assumption is justified persists (Sabach et al. 2017; Grichener et al. 2018; Ivanova 2018). Another candidate additional energy source is the fraction of energy released to the envelope as gas accretes onto the secondary (Soker 2004; Nordhaus & Blackman 2006; Ricker & Taam 2008, 2012; MacLeod et al. 2017; Moreno Méndez et al. 2017; Murguia-Berthier et al. 2017; Soker 2017; Shiber & Soker 2018; Paper I) but it is not yet clear how far into the CE such accretion would be be sustained.

Sources (or sinks) of energy not included in our simulation may play a role, and should be investigated further. But we must also assess how numerical limitations on the fidelity and parameter ranges of stellar models may contribute to inhibiting envelope ejection.

7.1 Restrictions on the available parameter space imposed by numerical limitations

Most CEE simulations to date involve RGB stars as they are numerically more tractable than those with AGB stars. The latter have comparably dense cores, but larger and more distended envelopes. This requires larger initial orbital separations and longer dynamical timescales. Notable exceptions involving AGB primaries are Sandquist et al. (1998) and Staff et al. (2016).

As discussed in Sec. 6.3, and supported Tab. 4, the final separation needed to eject a low mass primary RGB envelope after CEE is likely $\lesssim 1\,\mathrm{R}_\odot$. This does depend somewhat on parameter values: a_f would be expected to increase with M_2 (see equations (2) and (3) and the discussion preceding Sec. 6.2). The softening length $\gtrsim 1\,\mathrm{R}_\odot$, but halving the (spline) softening length at $t = 16.7$ d from $2.4\,\mathrm{R}_\odot$ to $1.2\,\mathrm{R}_\odot$ affected the orbit and drove mass inflow toward the secondary. This, despite a exceeding five softening lengths at that time, which was a proposed convergence criterion used by Ohlmann et al. 2016). This suggests that our simulation is not fully converged with respect to the softening length. Sandquist et al. (1998) and Iaconi et al. (2018) reached similar conclusions. It may also be that decreasing the softening length during the simulation provides less fidelity than a hypothetical simulation for which the softening length is kept constant at its smallest value from $t = 0$.[4]

CEE convergence studies are needed. Too-large softening length or inadequate resolution near the particles can cause artificial stagnation of $\dot{a}$ for small a. For real systems a would decay more rapidly than in the simulations, eventually ending in envelope ejection and/or ending in merger. However, large softening lengths also make the particles larger, and particle mergers *do* occur in some simulations (Iaconi et al. 2018), though this does not imply that such systems would necessarily merge in nature.

Some final separations from simulations are observed to be comparable to the observed separations of some close binaries (see, e.g. Gianninas et al. 2014) but the concept that numerical limitations stall orbital decay is overall supported when comparing final separations for simulations and observations compiled from the literature and presented in Fig. 15 of Iaconi et al. (2017) (see also De Marco et al. 2008). For small enough observed binary separation, it also is hard to know whether the CEE progenitors were RGB or AGB systems. This hypothesis could be addressed in the future by a statistical analysis that determines the relative likelihood of a given progenitor system for each observed post-CE binary system.

7.2 CEE simulations involving AGB stars

As mentioned above, global 3D simulations have so far focussed on systems involving RGB primaries, which are more compact than their AGB counterparts, and hence have a larger (in magnitude) binding energy. It follows that the final separation needed for envelope ejection for CEE involving an AGB primary should be significantly larger than for CEE involving an RGB primary, for equal mass companions (Tab. 4).

To explore this, we computed the AG energy terms from a ZAMS $2\,\mathrm{M}_\odot$ MESA (Paxton et al. 2011, 2013, 2015) AG/CE simulation, as presented in the sixth and seventh columns of Tab. 2 for initial separations just outside the AG surface and at the Roche limit separation, respectively: $a_\mathrm{i} = 124\,\mathrm{R}_\odot$ (compared to the AG radius of $122\,\mathrm{R}_\odot$) or $284\,\mathrm{R}_\odot$, computed from equation (4). We used the same procedure to calculate the modified stellar density and pressure profiles inside the cutoff radius for the AG as we did fort the RG and the same cutoff radius of $2.4\,\mathrm{R}_\odot$ (equal to the spline softening length) was chosen (see Ohlmann et al. 2017 and Paper I for details). This results in an AG of mass $1.8\,\mathrm{M}_\odot$ with a $0.5\,\mathrm{M}_\odot$ core (compared to $2.0\,\mathrm{M}_\odot$ and $0.4\,\mathrm{M}_\odot$ for the total mass and core mass of the RG). As seen in Tab. 2, the total initial energy of the envelope is indeed much smaller in magnitude for the AG than for the RG, which is also helped by the larger initial separation a_i.

The predicted values of a_f is also shown in Tab. 4 We see that

[4] The latter is difficult to achieve in practice since the volume resolved at the highest refinement level is higher at the beginning of the simulation and the softening length must be resolved by some minimum number of cells to avoid other numerical problems.

a_f is predicted to be almost four times larger for CEE involving the AGB star than for the RGB star.

In the run discussed in this work, we initially resolve the entire RG, as well as the secondary and part of the surrounding ambient medium, at the highest resolution. This would be impractical for the AG, since the volume is 16 times larger. Instead, one could reduce the resolution outside of the core, and then increase it again at the stellar surface where the scale height drops. Compounding the challenge, the orbital period $T \propto \sqrt{a^3/(M_1+M_2)}$ from Kepler's law, and with a factor of 2.5 in a and 0.94 in mass, the period increases by a factor of four. We can thus expect an increase in duration of the simulation by at least this factor. The drag force for the AG is also expected to be weaker than for the RG given the smaller initial orbital speed and lower envelope density, which could further slow the spiral-in. Finally, a larger simulation domain is desirable, further constraining the ambient density to avoid a very large mass in the ambient medium.

Sandquist et al. (1998) and Staff et al. (2016). Sandquist et al. (1998) performed five CEE simulations with AGB primaries of $3\,M_\odot$ or $5\,M_\odot$, and companions of $0.4\,M_\odot$ or $0.6\,M_\odot$. They used a nested grid approach with smallest resolution element $\delta = 2.2\,R_\odot$ and a Ruffert (1993) potential with smoothing length 1.5δ. They found final separations between $4\,R_\odot$ and $9\,R_\odot$, but deemed them to be upper limits due to sensitivity to resolution and smoothing length. Smaller smoothing lengths and higher resolution produced smaller final separations. Nevertheless, Iaconi et al. (2017) estimate that $\sim$ 21–46% of the envelope mass is unbound by the end of the Sandquist et al. (1998) simulations.

Most of the simulations carried out by Staff et al. (2016), meanwhile, consisted of a $3.05\,M_\odot$ $473\,R_\odot$ AGB primary (ZAMS $3.5\,M_\odot$) in an initially eccentric orbit with a secondary of mass $1.7\,M_\odot$. Comparing their simulations 4 and 4hr, with resolutions $\delta = 25\,R_\odot$ and $12\,R_\odot$, respectively, and smoothing length of $39\,R_\odot$ (Ruffert 1993) for both runs, they obtain final separations of $86\,R_\odot$ and $43\,R_\odot$, respectively, showing that a_f has not converged with resolution. They therefore report the $\sim$ 10% fraction of mass unbound at the end of their simulations to be a lower limit (for the definition $\mathcal{E}_{\rm gas} \geqslant 0$).

Interestingly, both Sandquist et al. (1998) and Staff et al. (2016) find *multiple* mass loss events, between periods of little unbinding. The initial unbinding event is nearly contemporaneous with first periastron passage, analogous to what is seen in most CEE simulations involving RGB stars. It takes a longer time interval of quiescence until the second unbinding event, followed by another quiescent phase. In Staff et al. (2016) this second event occurs around the time of second periastron passage, but in Sandquist et al. (1998) it happens much later. In any case, it would be interesting to explore how much mass becomes unbound in AGB/CEE simulations using AMR at much higher resolution near the particles, than in existing AGB/CEE simulations.

7.3 Redistribution of energy by convection

Convection operates within certain radial zones in real RGB and AGB stars, continuing through the CE phase, but simulations have so far not been realistic enough to capture it. Its absence is important: although convection is associated with a net outward heat flux it also also enhances diffusive mixing.

For optically thick regions, this mixing could increase $\alpha_{\rm CE}$ and $\widetilde{\alpha}_{\rm CE}$ by redistributing energy from the "rich" to the "poor" increasing the fraction of mass that is unbound. For example, during plunge-in, convection could transport some bulk kinetic and internal energy from the vicinity of particle 2 to the deeper more bound layers of the envelope, assisting envelope removal. For optically thin conditions, convection could have the opposite effect and reduce $\alpha_{\rm CE}$ (Wilson & Nordhaus 2018) by transporting energy near the secondary to the envelope surface, where it would be radiated away.

We can estimate whether convection would be important by comparing the timescale for convective mixing $t_{\rm conv}$ with the timescale for material encountered by the secondary to advect outward $t_{\rm adv}$. We estimate the diffusion mixing coefficient as $\eta = \xi c_{\rm s} H$, where $c_{\rm s}$ is the sound speed in the convection zone, H is the pressure scale height and $1/10 \leqslant \xi \leqslant 1/3$ is a constant of mixing length theory. The mixing time over a distance H would then be

$$t_{\rm conv} \sim \frac{H^2}{\eta} = \frac{H}{\xi c_{\rm s}}. \tag{5}$$

The timescale for the material to be advected over the same distance would be

$$t_{\rm adv} \sim \frac{H}{v_r}, \tag{6}$$

where v_r is a typical radial speed of outward-moving material. For convection to be important, we then require

$$v_r \lesssim \xi c_{\rm s}. \tag{7}$$

Part of the envelope meets this condition throughout the simulation.

It will be important to simulate CEE with a RGB or AGB primary envelope that is properly convectively unstable. The most direct way to achieve this is by using a more realistic equation of state that preserves an accurate temperature gradient. Ohlmann et al. (2017) show that using an ideal gas equation of state as we have done and others usually do, leads to a convectively stable envelope, even if the 1D simulation output used for the initial condition is convectively unstable. Alternatively, one could apply random forcing that converts internal energy into random bulk motions to mimic the mixing produced by convection.

8 SUMMARY AND CONCLUSIONS

This work can be divided into three main parts. In the first part (Sections 3 and 4), we analyze the energy budget in our simulation of CEE. The key findings are as follows:

- As with previous work, the CEE can be divided into a plunge-in phase whose termination approximately coincides with the first periastron passage, and a slow spiral-in phase. The transition between phases occurs when the secondary and its trailing tidal tail collide with the posterior tidal bulge of the primary. Further analysis of the orbital dynamics, including a measurement of the drag force and comparison with theory, is warranted.
- There is little net energy transfer between the orbital energy of particles (giant core and companion) and the binding energy of gas through the end of the dynamical plunge-in phase (t = 0 to 13 d), but the transfer is sufficient to unbind 14% of the envelope by t = 13 d. This is because the secondary gains a stronger hold on material in the inner envelope but energizes and ejects material in the outer envelope.
- Conversely, after the plunge-in until the end of the simulation (t = 13 to 40 d), energy is steadily transferred from particles to gas but little gas from the initially more tightly bound inner layers becomes unbound. It remains inconclusive as to whether a much longer run would lead to further unbinding.
- We find that the choice of ambient medium is important in determining the slope of the change in unbound mass with time

after plunge-in. This is not merely a numerical issue, but highlights the importance of the interaction between the envelope and its environment in determining how much mass gets unbound.

In the second part of the study (Sec. 5) we explored the relative motion of the centres of mass of the particles and gas:

- We calculated the relative motion of the particles CM and that of the envelope resulting from gas ejection near the secondary as it spirals inward. At the end of the simulation the particle CM moves steadily at $4\,\mathrm{km\,s^{-1}}$ with respect to the simulation frame (and $6\,\mathrm{km\,s^{-1}}$ in the gas CM frame), almost parallel to the orbital plane. This motion does not drastically change the level of unbinding compared to ignoring it but offers an explanation for the previously unexplained observed offsets between PN binary central stars and the geometric centres of their nebulae.

In the third part of the study (Secs. 6 and 7) we offer improvements to the energy formalism characterizing unbinding in CEE, compare the theory to simulations, and discuss the limits of simulations. The key points are:

- We introduce a conceptually cleaner version of the CE energy formalism (equations 3 and B4) wherein the $\widetilde{\alpha}_{\rm CE}$ parameter represents the efficiency of converting particle orbital energy to gas (un)binding energy. We discuss why $\widetilde{\alpha}_{\rm CE} \leqslant 1$ by construction, whereas the standard framework awkwardly allows $\alpha_{\rm CE} > 1$, confounding its physical meaning.
- We show that to eject the envelope with $\alpha_{\rm CE}$ or $\widetilde{\alpha}_{\rm CE} \leqslant 0.25$, we would, for our ZAMS $2\,\mathrm{M_\odot}$ RGB star + $1\,\mathrm{M_\odot}$ secondary system, need to evolve the simulation to a final inter-particle separation $a_{\rm f} \leqslant 0.9\,\mathrm{R_\odot}$, which is currently inaccessible to simulations due to numerical limitations.
- For a ZAMS $2\,\mathrm{M_\odot}$ AGB star + $1\,\mathrm{M_\odot}$ secondary, our predicted final separation for $\alpha_{\rm CE}$ and $\widetilde{\alpha}_{\rm CE} \leqslant 0.25$ is $a_{\rm f} < 3\,\mathrm{R_\odot}$, which may be accessible with current simulation methods. The larger length and time scales involved place a different set of demands on simulations involving AGB stars, but more CE simulations involving AGB primaries should be a priority.
- That the envelope remains mostly bound at the end of our simulation agrees with our theoretical expectation, given the physics and numerical parameters of the simulations.
- While we cannot say for sure what much longer simulations will bring, exacerbating envelope unbinding may benefit from the following: (1) additional energy sources (e.g. recombination energy, accretion energy), or (2) improved numerical reliability at low inter-particle separations; (3) improved realism of energy transport in the stellar models that may diffusively redistribute the envelope energy such that a larger fraction of mass has just enough energy to remain unbound.
- Convection is the most likely possible contributor to the latter and is known to occur in RGB and AGB stars, though it remains to be seen whether the associated change in the unbinding efficiency (as embodied in the parameter $\alpha_{\rm CE}$ or $\widetilde{\alpha}_{\rm CE}$) would be toward enhanced or reduced efficiency. In any case, developing CE simulations that include convection is critical in our view, and the most natural and direct path toward this goal would involve implementing more realistic equations of state such that the temperature gradients of the giant stars are faithfully reproduced (Ohlmann et al. 2017).

Many challenges remain for simulating CEE. Progress will require improvements in the numerics (initial conditions, resolution, refinement strategy) as well as the inclusion of more physics (convection, radiative transport, recombination, jet feedback).

ACKNOWLEDGEMENTS

LC thanks Orsola De Marco, Paul Ricker, Sebastian Ohlmann and Thomas Reichardt for stimulating and helpful discussions. We acknowledge support form National Science Foundation (NSF) grants AST-1515648 and AST-1813298. This work used the Extreme Science and Engineering Discovery Environment (XSEDE), which is supported by NSF grant number ACI-1548562. The authors acknowledge the Texas Advanced Computing Center (TACC) at The University of Texas at Austin for providing HPC resources (through XSEDE allocation TG-AST120060) that have contributed to the research results reported within this paper.

References

Briggs G. P., Ferrario L., Tout C. A., Wickramasinghe D. T., 2018, MNRAS, 481, 3604
Carroll-Nellenback J. J., Shroyer B., Frank A., Ding C., 2013, Journal of Computational Physics, 236, 461
Chamandy L., et al., 2018, MNRAS, 480, 1898
Clayton M., Podsiadlowski P., Ivanova N., Justham S., 2017, MNRAS, 470, 1788
Clyne N., Redman M. P., Lloyd M., Matsuura M., Singh N., Meaburn J., 2014, A&A, 569, A50
Cojocaru R., Rebassa-Mansergas A., Torres S., García-Berro E., 2017, MNRAS, 470, 1442
Cunningham A. J., Frank A., Varnière P., Mitran S., Jones T. W., 2009, ApJS, 182, 519
Davis P. J., Kolb U., Willems B., 2010, MNRAS, 403, 179
De Marco O., Hillwig T. C., Smith A. J., 2008, AJ, 136, 323
Dewi J. D. M., Tauris T. M., 2001, in Podsiadlowski P., Rappaport S., King A. R., D'Antona F., Burderi L., eds, Astronomical Society of the Pacific Conference Series Vol. 229, Evolution of Binary and Multiple Star Systems. p. 255
Eggleton P. P., 1983, ApJ, 268, 368
Gianninas A., Dufour P., Kilic M., Brown W. R., Bergeron P., Hermes J. J., 2014, ApJ, 794, 35
Grichener A., Sabach E., Soker N., 2018, preprint, (arXiv:1803.05864)
Hillwig T. C., Jones D., De Marco O., Bond H. E., Margheim S., Frew D., 2016, ApJ, 832, 125
Iaconi R., Reichardt T., Staff J., De Marco O., Passy J.-C., Price D., Wurster J., Herwig F., 2017, MNRAS, 464, 4028
Iaconi R., De Marco O., Passy J.-C., Staff J., 2018, MNRAS, 477, 2349
Ivanova N., 2018, ApJ, 858, L24
Ivanova N., Nandez J. L. A., 2016, MNRAS, 462, 362
Ivanova N., et al., 2013, ARA&A, 21, 59
Jones D., et al., 2010, MNRAS, 408, 2312
Jones D., Boffin H. M. J., Rodríguez-Gil P., Wesson R., Corradi R. L. M., Miszalski B., Mohamed S., 2015, A&A, 580, A19
Livio M., Soker N., 1988, ApJ, 329, 764
MacLeod M., Antoni A., Murguia-Berthier A., Macias P., Ramirez-Ruiz E., 2017, ApJ, 838, 56
MacLeod M., Ostriker E. C., Stone J. M., 2018a, preprint, (arXiv:1808.05950)
MacLeod M., Ostriker E. C., Stone J. M., 2018b, ApJ, 863, 5
Miszalski B., Manick R., Mikołajewska J., Van Winckel H., Iłkiewicz K., 2018, PASA, 35, e027
Moreno Méndez E., López-Cámara D., De Colle F., 2017, MNRAS, 470, 2929
Murguia-Berthier A., MacLeod M., Ramirez-Ruiz E., Antoni A., Macias P., 2017, ApJ, 845, 173
Nandez J. L. A., Ivanova N., 2016, MNRAS, 460, 3992
Nandez J. L. A., Ivanova N., Lombardi Jr. J. C., 2014, ApJ, 786, 39
Nandez J. L. A., Ivanova N., Lombardi J. C., 2015, MNRAS, 450, L39
Nordhaus J., Blackman E. G., 2006, MNRAS, 370, 2004
Ohlmann S. T., Röpke F. K., Pakmor R., Springel V., 2016, ApJ, 816, L9

Ohlmann S. T., Röpke F. K., Pakmor R., Springel V., 2017, A&A, 599, A5
Passy J.-C., Mac Low M.-M., De Marco O., 2012, ApJ, 759, L30
Paxton B., Bildsten L., Dotter A., Herwig F., Lesaffre P., Timmes F., 2011, ApJS, 192, 3
Paxton B., et al., 2013, ApJS, 208, 4
Paxton B., et al., 2015, ApJS, 220, 15
Rasio F. A., Livio M., 1996, ApJ, 471, 366
Reichardt T. A., De Marco O., Iaconi R., Tout C. A., Price D. J., 2018, preprint, (arXiv:1809.02297)
Ricker P. M., Taam R. E., 2008, ApJ, 672, L41
Ricker P. M., Taam R. E., 2012, ApJ, 746, 74
Ruffert M., 1993, A&A, 280, 141
Sabach E., Hillel S., Schreier R., Soker N., 2017, MNRAS, 472, 4361
Sahai R., et al., 1999, AJ, 118, 468
Sandquist E. L., Taam R. E., Chen X., Bodenheimer P., Burkert A., 1998, ApJ, 500, 909
Sandquist E. L., Taam R. E., Burkert A., 2000, ApJ, 533, 984
Shiber S., Soker N., 2018, MNRAS,
Soker N., 2004, New Astron., 9, 399
Soker N., 2017, MNRAS, 471, 4839
Staff J. E., De Marco O., Macdonald D., Galaviz P., Passy J.-C., Iaconi R., Low M.-M. M., 2016, MNRAS, 455, 3511
Tutukov A., Yungelson L., 1979, in Conti P. S., De Loore C. W. H., eds, IAU Symposium Vol. 83, Mass Loss and Evolution of O-Type Stars. pp 401–406
Wilson E. C., Nordhaus J., 2018, preprint, (arXiv:1811.03161)
Zorotovic M., Schreiber M. R., Gänsicke B. T., Nebot Gómez-Morán A., 2010, A&A, 520, A86
de Kool M., 1990, ApJ, 358, 189
van den Heuvel E. P. J., 1976, in Eggleton P., Mitton S., Whelan J., eds, IAU Symposium Vol. 73, Structure and Evolution of Close Binary Systems. p. 35

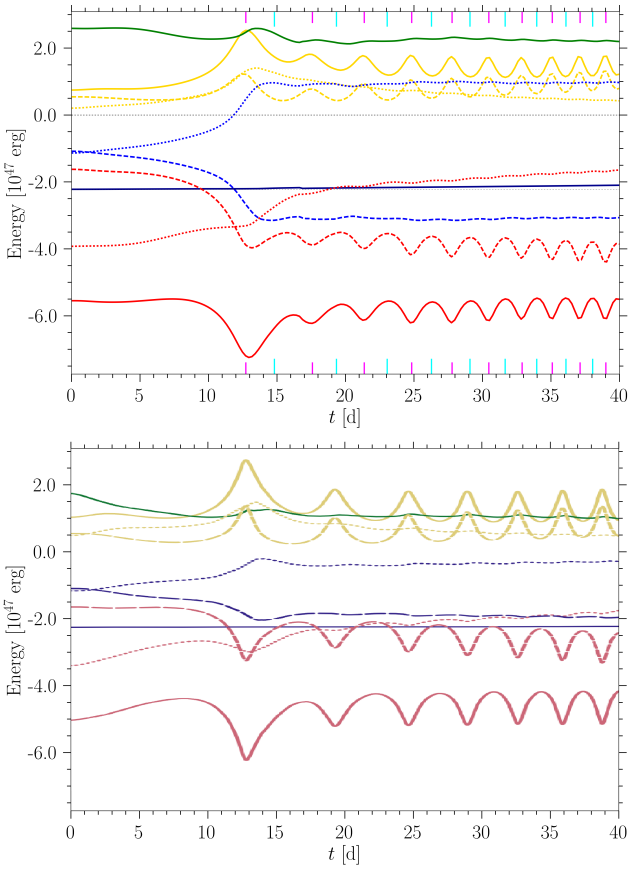

Figure A1. Comparison between energy terms (integrated over the simulation domain) in our simulation (top) and in the simulation of Ohlmann et al. (2016) (bottom, adapted from the latter work). Legend labels are the same as those of Ohlmann et al. (2016): 'total' (solid blue), 'kinetic' (solid yellow), 'potential' (solid red), 'internal' (solid green), 'total envelope' (dotted blue), 'kinetic envelope' (dotted yellow), 'potential envelope' (dotted red), 'total cores' (dashed blue), 'kinetic cores' (dashed yellow) and 'potential cores' (dashed red). In the upper panel the contribution from $E_{\rm pot,gas-1}$ is included in the envelope potential energy and total envelope energy but the contribution from $E_{\rm pot,gas-2}$ is not so included. On the other hand, the contribution from $E_{\rm pot,gas-2}$ is included in the cores potential energy and total cores energy, but these terms do not include the contribution from $E_{\rm pot,gas-1}$.

APPENDIX A: COMPARISON WITH PREVIOUS WORK

We used almost the same parameter values and initial conditions as Ohlmann et al. (2016) and thus it is useful to compare directly their results and ours. In the top panel of Fig. A1 we plot the energy terms as in Fig. 2 of Ohlmann et al. (2016), and in the bottom panel we show a version of their figure with the time axis truncated at $t = 40$ d. The curves are as described in the legend but Ohlmann et al. (2016) used a different kind of code and it was not entirely clear to us precisely how the different energy components were divided among the various curves. We found that close agreement was obtained if the curves labeled as envelope potential energy and total envelope energy (dotted red and dotted blue, respectively) include the contribution from $E_{\rm pot,gas-1}$ but not from $E_{\rm pot,gas-2}$, and the curves labeled as cores potential energy and total cores energy (dashed red and dashed blue, respectively) include the contribution from $E_{\rm pot,gas-2}$ but not from $E_{\rm pot,gas-1}$,

The Ohlmann et al. (2016) setup allowed for a much lower pressure and lower density ambient medium. Thus, to make a direct comparison with our simulation, it was necessary to subtract from each energy term the fraction contributed by the ambient medium (or by the gravitational interaction between the ambient medium and the other components); these quantities involving the ambient gas were assumed to remain constant for the duration of the simulation. The ambient energy inflow from the boundaries is measured to be negligible. As expected from the analysis of Paper I, close agreement between results from the two simulations is apparent, in spite of the very different methodologies used. There is, however, a larger separation between the total particle energy and total gas energy curves (shown in dashed blue and dotted blue, respectively) after plunge-in in the top panel of Fig. A1 as compared with the bottom panel. The particle and gas potential energies also experience larger changes during plunge-in (dashed and dotted red, respectively).

Assuming that our partitioning of the energy components mimics reasonably well that of Ohlmann et al. (2016), these differences could be caused by differences in initial conditions. Firstly, in our simulation the RG is not rotating with respect to the inertial frame of reference of the simulation, while in that of Ohlmann et al. (2016) the RG is initialized with a solid body rotation of 95% of the orbital angular speed. (The reality would lie somewhere in between and can be estimated as $\sim 30\%$ of the orbital angular speed from the results of MacLeod et al. 2018b). In spite of this difference, however, the inter-particle separation a reaches a smaller value ($< 10\,{\rm R}_\odot$) at the first periastron passage in the simulation of Ohlmann et al. (2016) than in that of Paper I ($14\,{\rm R}_\odot$), even though the time of this first periastron passage (i.e. the end of plunge-in, as we have defined it) occurs at about $t = 13$ d in both simulations.

Secondly, Ohlmann et al. (2016) performed a relaxation run to set up their initial condition, while we did not, which would have led to differences in the initial stellar profiles (apart from the slight differences that would have already existed due to the slightly different MESA models employed). We note that some quantities, like internal energy (solid green) and total potential energy (solid red) remain approximately constant for the first ~ 5 d in our simulation, while showing more variation in that of Ohlmann et al. (2016). This suggests that the RG is more stable in our simulation. Possible reasons are that we iterated over the RG core mass to obtain a smoother initial RG profile, we resolved the entire RG at the highest refinement level, and we used a denser and higher pressure ambient medium to stabilize the outer layers of the RG. The latter is a compromise since a larger ambient density and pressure complicates the analysis. Clearly, obtaining an initial

condition that is both highly stable and physically realistic in CE simulations is computationally challenging. In any case, we are encouraged by the close agreement between the two simulations, and take this as confirmation that our results are physical, as opposed to being dominated by numerical artefacts.

APPENDIX B: DERIVATION OF THE NEW ENERGY FORMALISM

Here we provide a brief derivation of the alternative CE EF, encapsulated by equation (3) or (B4). On the RHS we want $-\Delta E_{1-2} = -\Delta(E_{\rm pot,\,1-2}+E_{\rm bulk,\,1}+E_{\rm bulk,\,2})$, multiplied by the efficiency factor $\widetilde{\alpha}_{\rm CE}$, where Δ refers to final minus initial. The contribution $-(E_{\rm pot,\,1-2,\,f}+E_{\rm bulk,\,1,\,f}+E_{\rm bulk,\,2,\,f})$, where 'f' stands for final, is unchanged from equation (2) and is equal to $GM_{1,\rm c}M_2/(2a_{\rm f})$. On the LHS, we want the change in binding energy (defined to be positive) of the envelope. With the final binding energy assumed to be zero, we obtain $-(E_{\rm pot,\,gas-1,\,i}+E_{\rm pot,\,gas-gas,\,i}+E_{\rm int,\,gas,\,i}+E_{\rm bulk,\,gas,\,i}+E_{\rm pot,\,gas-2,\,i})$, with 'i' indicating initial. The contribution $-(E_{\rm pot,\,gas-1,\,i}+E_{\rm pot,\,gas-gas,\,i}+E_{\rm int,\,gas,\,i})$ is given by $GM_1M_{1,\rm e}/(\lambda R_1)$, and is unchanged from the standard treatment of equation (2).

We now derive the remaining terms, assuming the initial orbit to be circular, in accordance with the initial condition of the simulation. On the RHS, we have the contribution $E_{\rm pot,\,1-2,\,i}+E_{\rm bulk,\,1,\,i}+E_{\rm bulk,\,2,\,i}$. For a circular orbit, the velocities of particles 1 and 2 are, respectively, given by $v_1^2 = G\mu M_2/(aM_1)$ and $v_2^2 = G\mu M_1/(aM_2)$, with the reduced mass $\mu = M_1M_2/(M_1+M_2)$, so that

$$\begin{aligned} &E_{\rm pot,\,1-2,\,i}+E_{\rm bulk,\,1,\,i}+E_{\rm bulk,\,2,\,i}\\ &\quad=-\frac{GM_{1,\rm c}M_2}{a_{\rm i}}+\frac{GM_{1,\rm c}M_2\mu}{2a_{\rm i}M_1}+\frac{GM_2M_1\mu}{2a_{\rm i}M_2}\\ &\quad=-\frac{GM_{1,\rm c}M_2}{2a_{\rm i}}\left(2-\frac{\mu}{M_1}-\frac{M_1\mu}{M_{1,\rm c}M_2}\right)\\ &\quad=-\frac{GM_{1,\rm c}M_2}{2a_{\rm i}}\left(2-\frac{M_1^2/M_{1,\rm c}+M_2}{M_1+M_2}\right). \end{aligned} \tag{B1}$$

Now, for the LHS we are left to evaluate the contribution $-(E_{\rm bulk,\,gas,\,i}+E_{\rm pot,\,gas-2,\,i})$. This is given by

$$\begin{aligned} -(E_{\rm bulk,\,gas,\,i}+E_{\rm pot,\,gas-2,\,i}) &= -\frac{GM_{1,\rm e}M_2\mu}{2a_{\rm i}M_1}+\frac{GM_{1,\rm e}M_2}{a}\\ &=\frac{GM_{1,\rm e}M_2}{2a_{\rm i}}\left(2-\frac{\mu}{M_1}\right)=\frac{GM_{1,\rm e}M_2}{2a_{\rm i}}\left(2-\frac{M_2}{M_1+M_2}\right). \end{aligned} \tag{B2}$$

Now gathering together the various terms we arrive at the equation

$$\begin{aligned} &GM_{1,\rm e}\left[\frac{M_1}{\lambda R_1}+\frac{M_2}{2a_{\rm i}}\left(2-\frac{M_2}{M_1+M_2}\right)\right]\\ &\quad=\widetilde{\alpha}_{\rm CE}\frac{GM_{1,\rm c}M_2}{2}\left[\frac{1}{a_{\rm f}}-\frac{1}{a_{\rm i}}\left(2-\frac{M_1^2/M_{1,\rm c}+M_2}{M_1+M_2}\right)\right]. \end{aligned} \tag{B3}$$

Equation (3) can be derived from equation (B3) using straightforward algebra.

To gain insight, we can use $M_1 = M_{1,\rm c}+M_{1,\rm e}$ to rewrite the last term on the RHS of equation (3), and combine it with the last term on the LHS:

$$\begin{aligned} &GM_{1,\rm e}\left[\frac{M_1}{\lambda R_1}+\frac{M_2}{2a_{\rm i}}\left(1+(1-\widetilde{\alpha}_{\rm CE})\frac{M_1}{M_1+M_2}\right)\right]\\ &\quad=\widetilde{\alpha}_{\rm CE}\frac{GM_{1,\rm c}M_2}{2}\left(\frac{1}{a_{\rm f}}-\frac{1}{a_{\rm i}}\right). \end{aligned} \tag{B4}$$

On the right side of equation (B4) we have the orbital energy that would have been released by the particles had the envelope mass been negligible. The term proportional to M_2 on the LHS is comprised of three contributions: (i) the part $GM_{1,\rm e}M_2/2a_{\rm i}$ corresponds to negative the initial orbital energy of the envelope–particle 2 subsystem, neglecting the effect of particle 1, (ii) the part with the same form as (i) but multiplied by $M_1/(M_1+M_2)$ accounts for the decrement in initial kinetic energy of the envelope, as compared to (i), caused by the finite mass of particle 1, and (iii) the part with the same form as (ii) (but multiplied by $-\widetilde{\alpha}_{\rm CE}$) accounts for the extra kinetic energy of particle 2 due to the presence of the envelope. The appearance of parts (ii) and (iii) stems from the need to separate out particle 2 and envelope kinetic energy contributions, since only particle energy terms should be multiplied by $\widetilde{\alpha}_{\rm CE}$ in our version of the formalism. For the case $\alpha = \widetilde{\alpha}_{\rm CE} = 1$, there is no longer any need to distinguish between these contributions, parts (ii) and (iii) cancel out, and equations (B4) and (2) become equivalent.